Supporting Information

Rapid Cycling and Exceptional Yield in a Metal-Organic Framework Water Harvester

Nikita Hanikel,[†,‡] Mathieu S. Prévot,[†,‡] Farhad Fathieh,[†] Eugene A. Kapustin,[†] Hao Lyu,[†] Haoze Wang,[†] Nicolas J. Diercks,[†] T. Grant Glover,[§] and Omar M. Yaghi*[,†,⊥]

[†]Department of Chemistry, University of California-Berkeley; Materials Sciences Division, Lawrence Berkeley National Laboratory; Kavli Energy NanoSciences Institute; and Berkeley Global Science Institute, Berkeley, California 94720, United States

[§]Department of Chemical and Biomolecular Engineering, University of South Alabama, Mobile, Alabama 36688, United States

[⊥]UC Berkeley-KACST Joint Center of Excellence for Nanomaterials for Clean Energy Applications, King Abdulaziz City for Science and Technology, Riyadh 11442, Saudi Arabia

[‡]Equal contribution

Table of Contents

Section S1. Material Synthesis and Preparation

MOF-303 Synthesis

3,5-pyrazoledicarboxylic acid, monohydrate (7.50 g, 43.1 mmol, Crysdot LLC, 97% purity) was dissolved in deionized H_2O (725 mL) and LiOH solution (2.57 M, 25 mL, Fisher Scientific, 98% purity). The resulting solution was heated for 30 min in a pre-heated oven at 120 °C. Afterwards, $AlCl_3 \cdot 6H_2O$ (10.4 g, 43.1 mmol, Sigma Aldrich Co, ≥ 99.8% purity) was added to the solution. Any precipitate was dissolved under sonication and vigorous shaking. Once a clear solution was obtained, the hot reaction mixture was put in a pre-heated oven at 100 °C, where it was kept for 15 hours. Then, the precipitate was filtrated out and washed with water. The snow-white solid was subsequently washed with MeOH (anhydrous, Macron Fine Chemicals) for 24 hours in a Soxhlet apparatus and air-dried for 3 days. Further, the product was dried under dynamic vacuum ($<10^{-2}$ mbar) for 24 hours. Full activation of the MOF was conducted under dynamic vacuum ($\sim10^{-3}$ mbar) and at 150 °C for 6 hours, yielding pure, desolvated product (3.6 g).

Aluminum Fumarate Synthesis

Large-scale synthesis of Al-fumarate was conducted according to a previously reported procedure.[1] For the material comparison study, Al-fumarate was synthesized in higher quality (larger crystallite size — comparable to MOF-303, and minimal to no hysteresis between water vapor ad- and desorption according to SEM and water sorption analysis, respectively). For this purpose, fumaric acid (66.7 mg, 0.575 mmol, Sigma Aldrich Co, ≥ 99% purity) and $AlCl_3 \cdot 6H_2O$ (139 mg, 0.575 mmol, Sigma Aldrich Co, ≥ 99.8% purity) were dissolved in KOH solution (0.086 M, 10 mL, Fisher Scientific, ≥ 85% purity). The resulting clear solution was incubated in a pre-heated 100 °C oven for 12 hours, which resulted in precipitation of a white crystalline powder. The product was washed five times over one day with H_2O (15 mL each time) and another five times over a second day with MeOH (15 mL each time).

SAPO-34 (ACS Material, LLC) and zeolite 13X (Alfa Aeser) were commercially attained.

Prior to sorption measurements and gas pycnometry, the samples were activated under dynamic vacuum ($\sim10^{-3}$ mbar) and at elevated temperatures. The MOF samples were activated at 150 °C for 6 hours, SAPO-34 at 180 °C for 12 hours and zeolite 13X at 225 °C for 12 hours.

Section S2. Material Characterization

Section S2.1. Powder X-Ray Diffraction Analysis

Powder X-ray diffraction (PXRD) patterns were recorded with a Bruker D8 Advance diffractometer (Bragg-Brentano geometry, Cu Kα1 radiation).

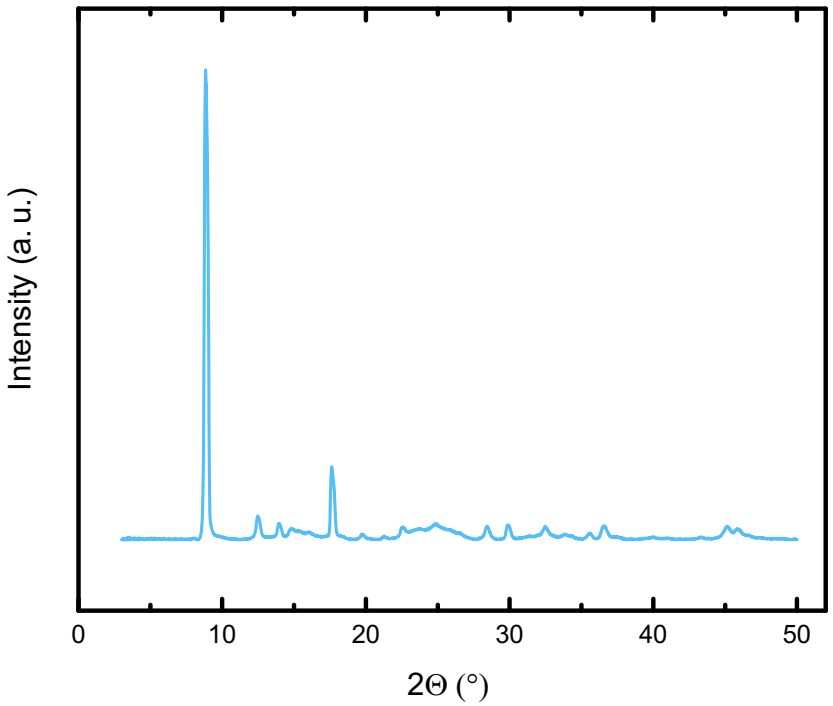

Figure S1. Experimental powder X-ray diffraction pattern of MOF-303 (λ = 1.5418 Å).

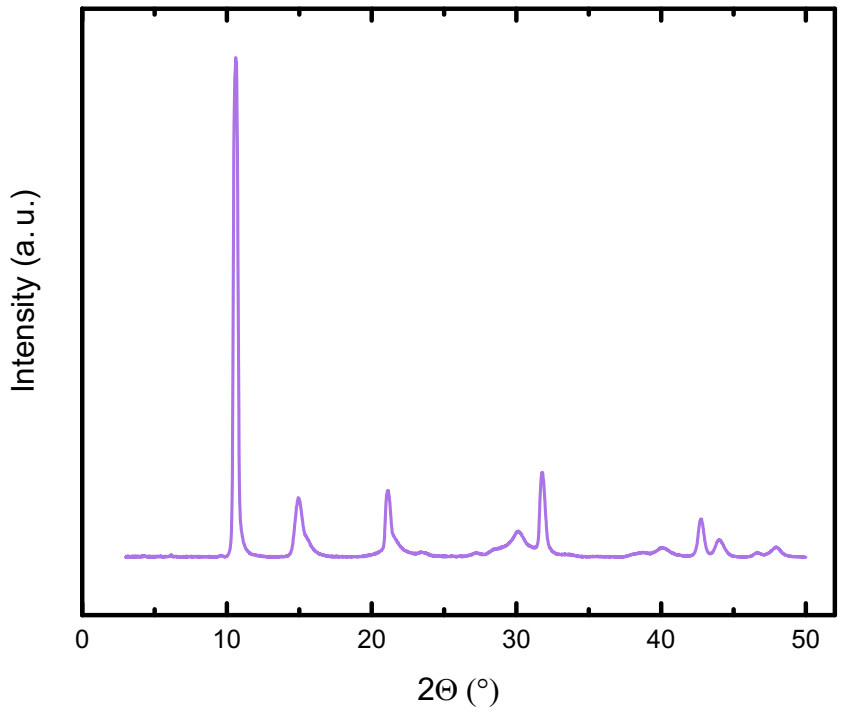

Figure S2. Experimental powder X-ray diffraction pattern of Al-fumarate (λ = 1.5418 Å).

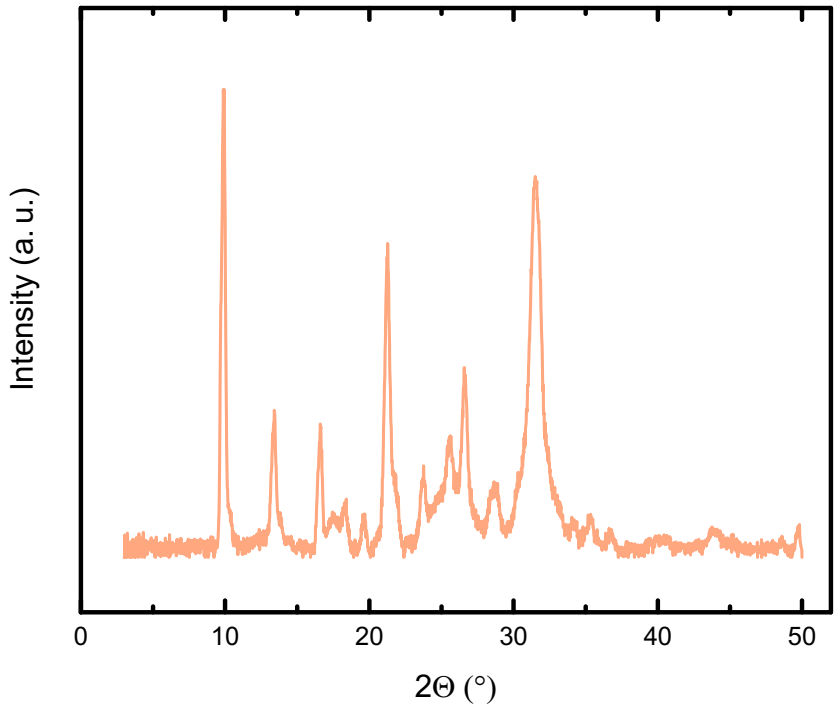

Figure S3. Experimental powder X-ray diffraction pattern of SAPO-34 (λ = 1.5418 Å).

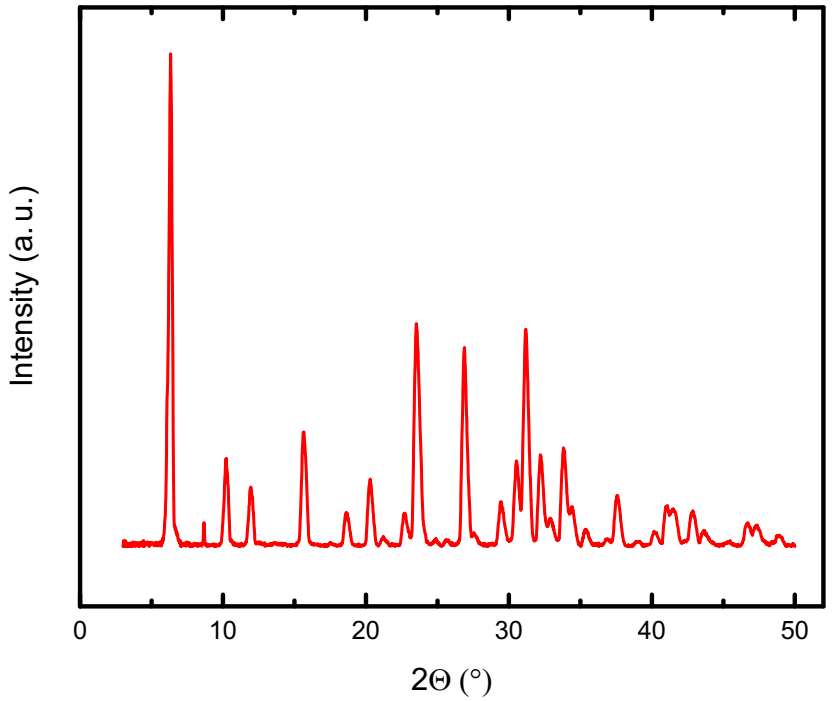

Figure S4. Experimental powder X-ray diffraction pattern of zeolite 13X (λ = 1.5418 Å).

Section S2.2. Scanning Electron Microscopy

Scanning electron microscopy (SEM) images were recorded with a FEI Quanta 3D FEG scanning electron microscope (10 kV accelerating voltage and 10.8 mm working distance).

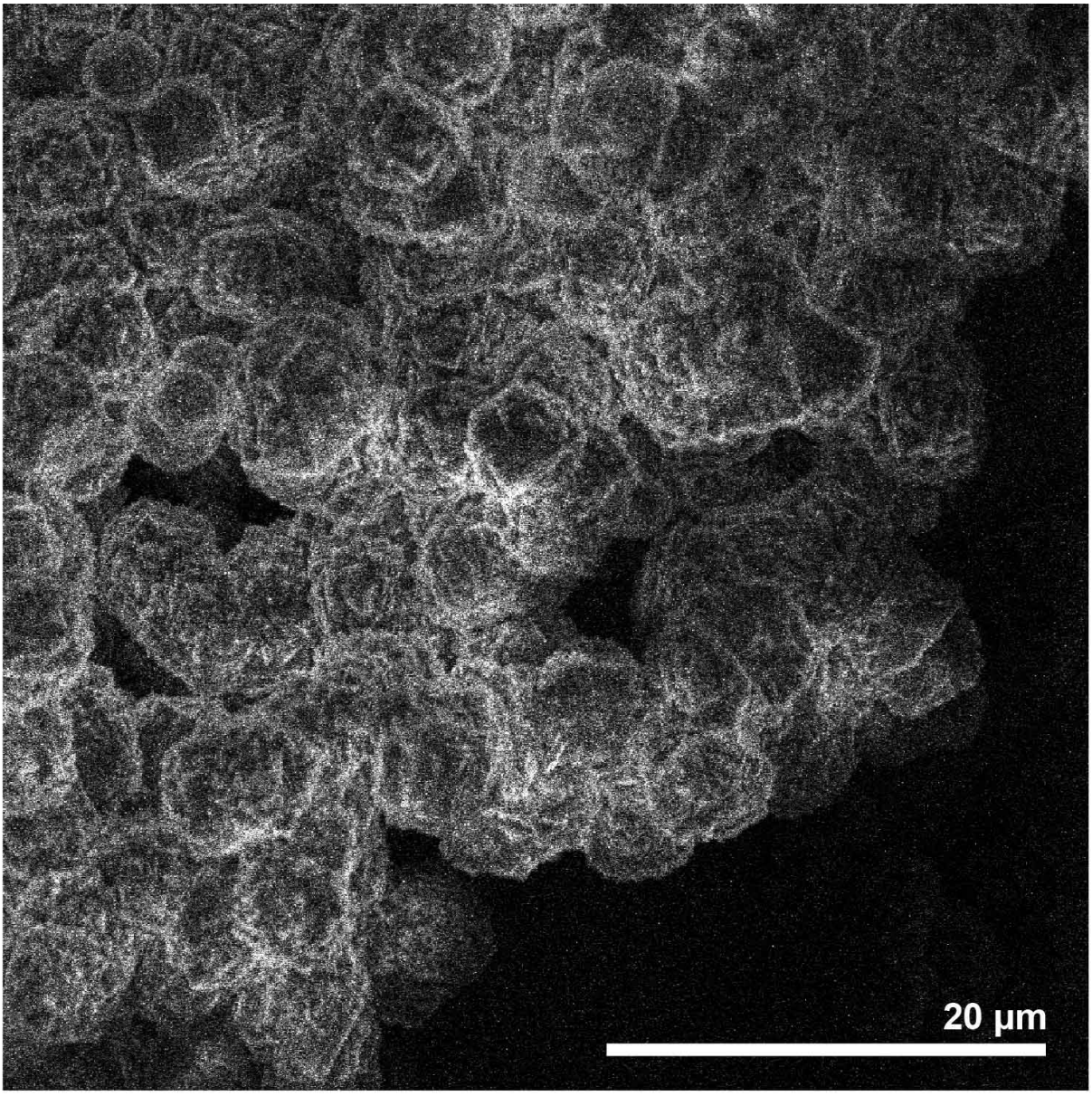

Figure S5. Representative scanning electron microscopy micrograph of MOF-303 crystallites used for the dynamic water sorption study (after synthesis, washing and activation).

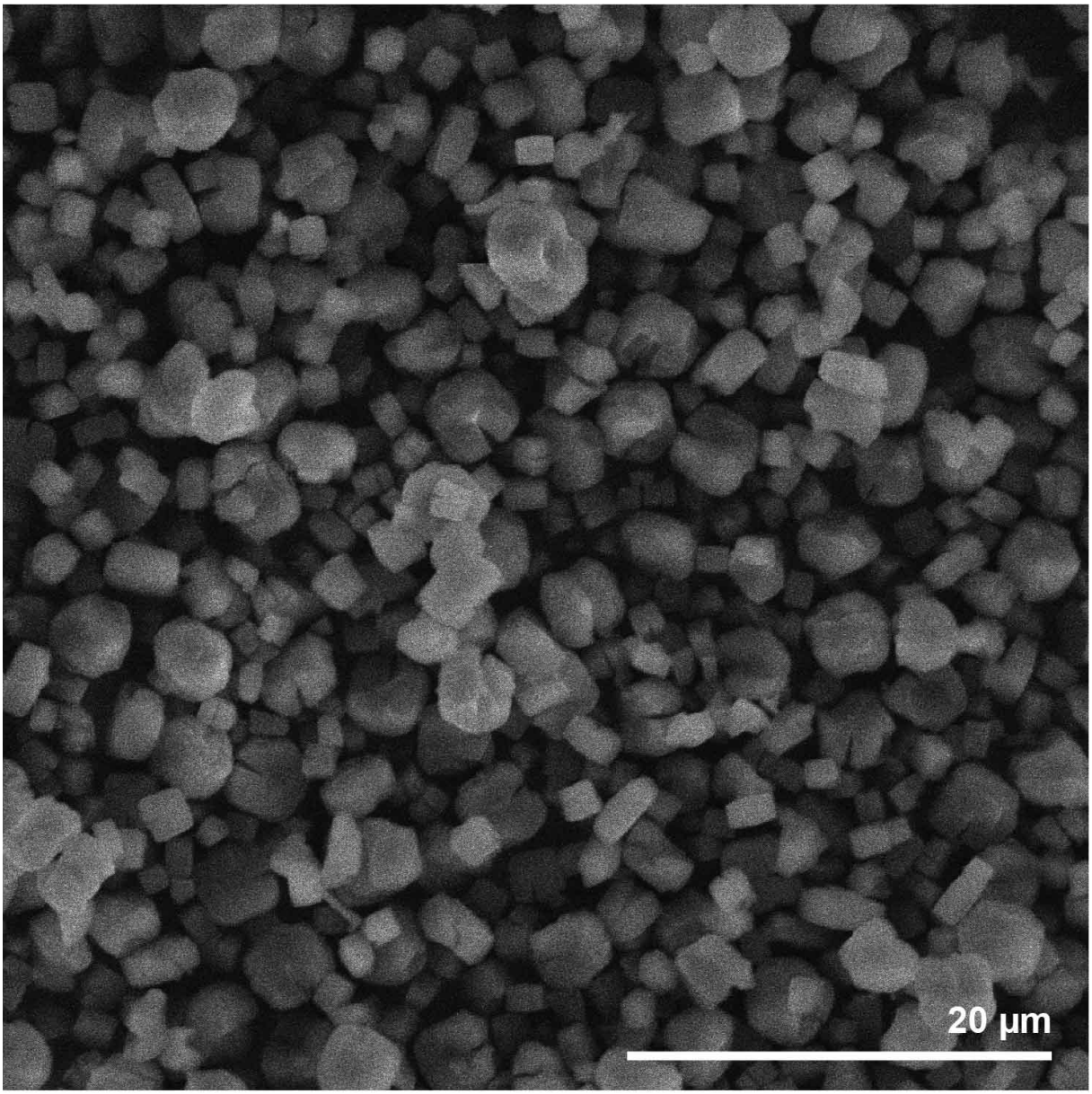

Figure S6. Representative scanning electron microscopy micrograph of Al-fumarate crystallites used for the dynamic water sorption study (after synthesis, washing and activation).

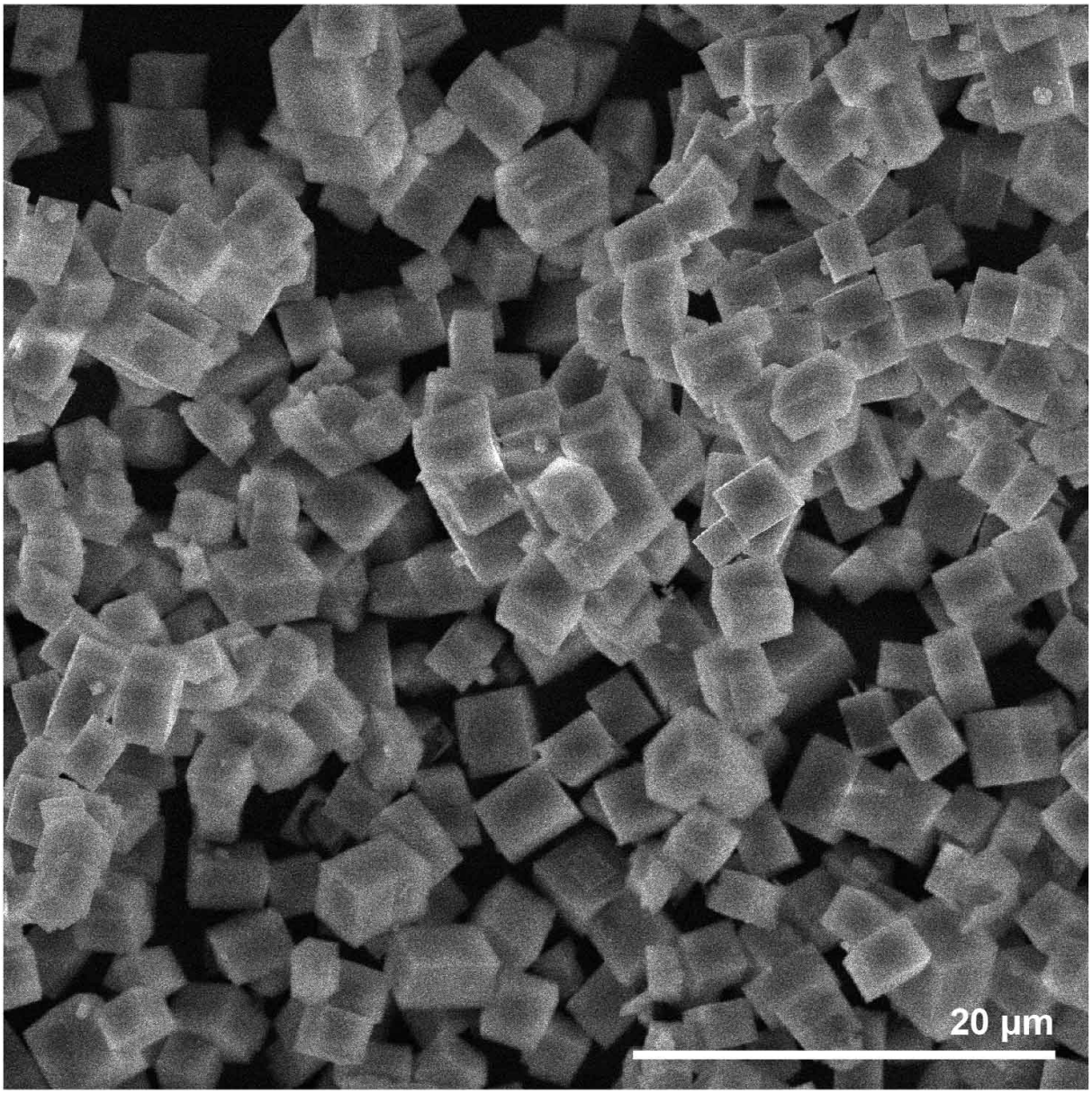

Figure S7. Representative scanning electron microscopy micrograph of SAPO-34 crystallites used for the dynamic water sorption study (after synthesis, washing and activation).

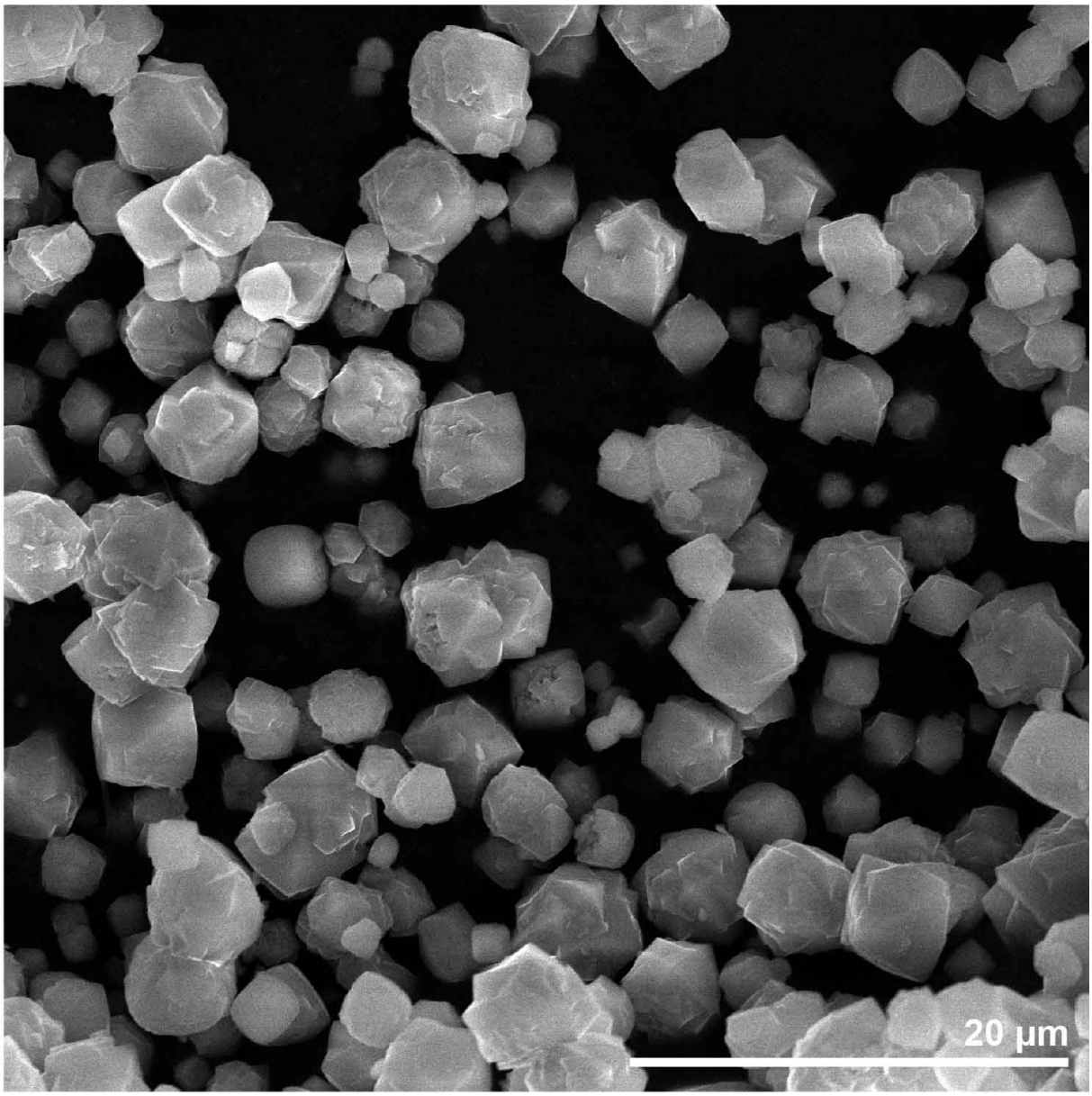

Figure S8. Representative scanning electron microscopy micrograph of zeolite 13X crystallites used for the dynamic water sorption study (after synthesis, washing and activation).

Section S2.3. Argon Sorption Analysis

Argon (Praxair, ultrahigh purity, 99.999%) sorption isotherms were recorded on a Quantachrome AUTOSORB-1 volumetric gas adsorption analyzer. A liquid argon bath (87 K) was used for these measurements. Ultrahigh-purity helium (Praxair, 99.999%) was used for dead space estimation.

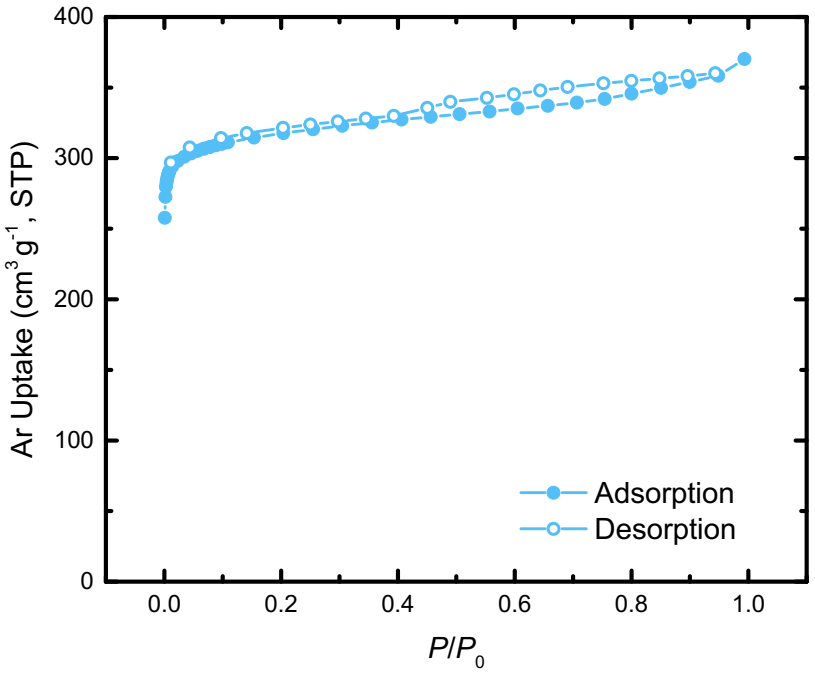

Figure S9. Linear plot of the argon sorption isotherm of MOF-303 at 87 K (P: partial pressure of argon, P_0 = 1 atm). BET surface area: 1119 m^2 g^{-1}.

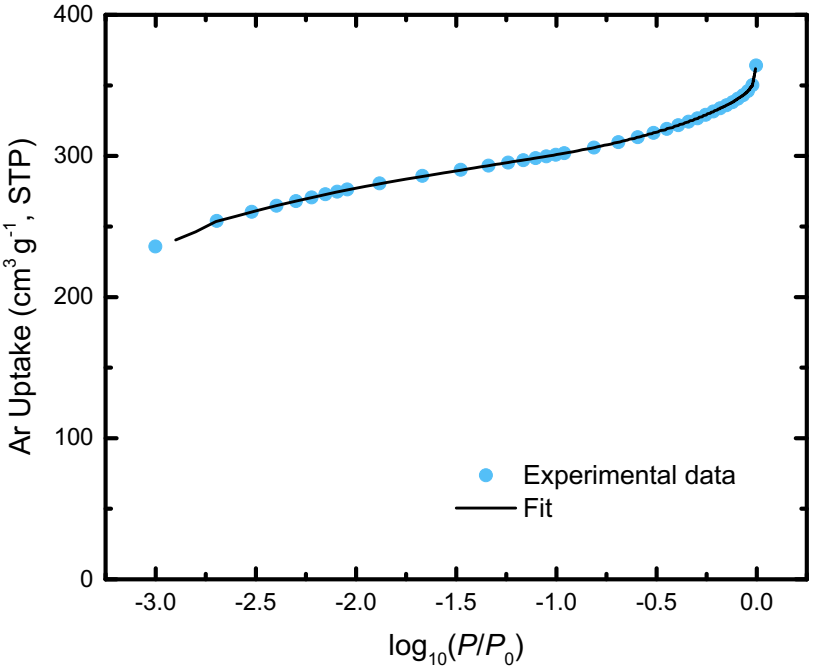

Figure S10. Logarithmic plot of the adsorption branch of the argon sorption isotherm of MOF-303 at 87 K (P: partial pressure of argon, P_0 = 1 atm) and fitting comparison with a NLDFT model (adsorption branch, argon on zeolites at 87 K, cylindrical pores, fitting error = 0.037%).

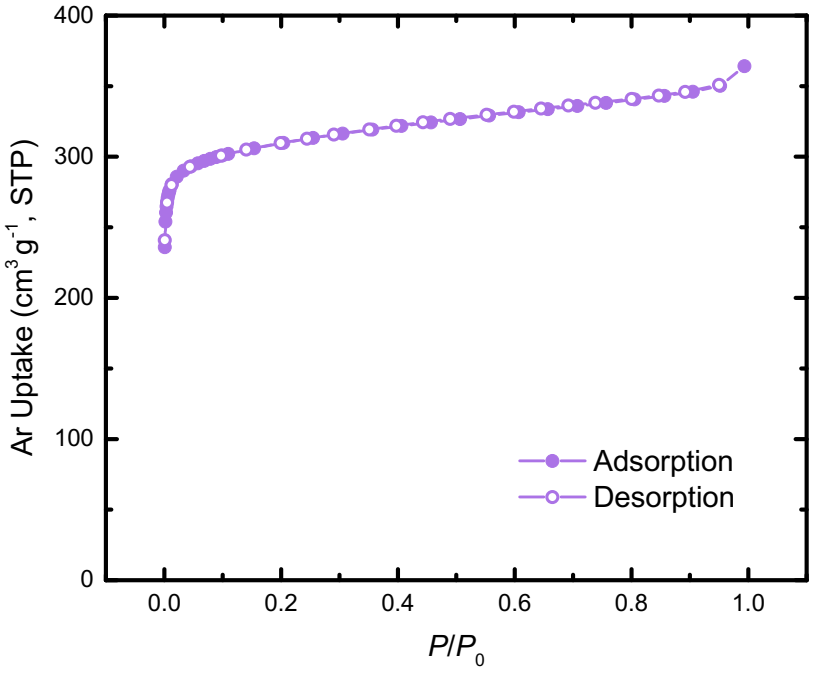

Figure S11. Linear plot of the argon sorption isotherm of Al-fumarate at 87 K (*P*: partial pressure of argon, P_0 = 1 atm). BET surface area: 1080 m^2 g^{-1}.

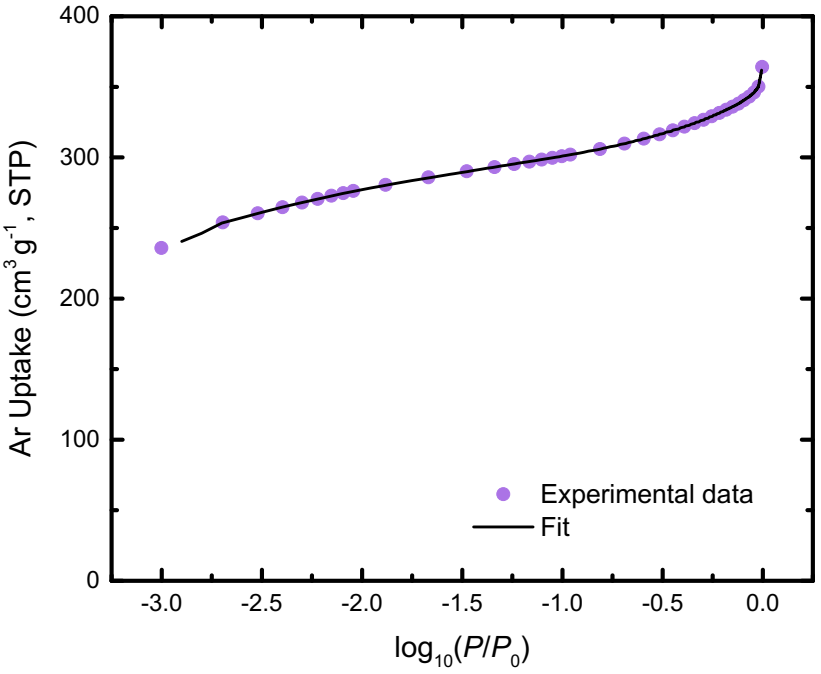

Figure S12. Logarithmic plot of the adsorption branch of the argon sorption isotherm of Al-fumarate at 87 K (*P*: partial pressure of argon, P_0 = 1 atm) and fitting comparison with a NLDFT model (adsorption branch, argon on zeolites at 87 K, cylindrical pores, fitting error = 0.033%).

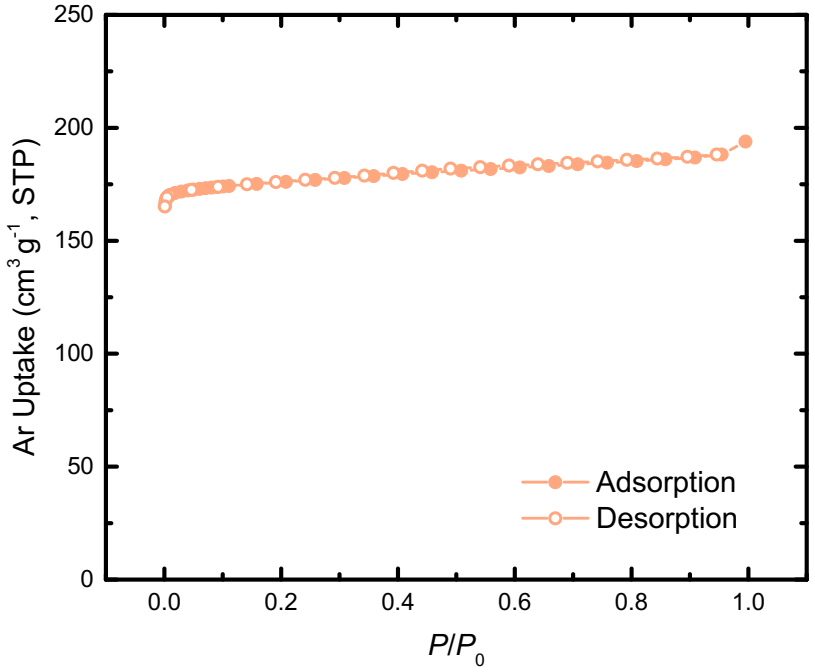

Figure S13. Linear plot of the argon sorption isotherm of SAPO-34 at 87 K (*P*: partial pressure of argon, P_0 = 1 atm). BET surface area: 931 m^2 g^{-1}.

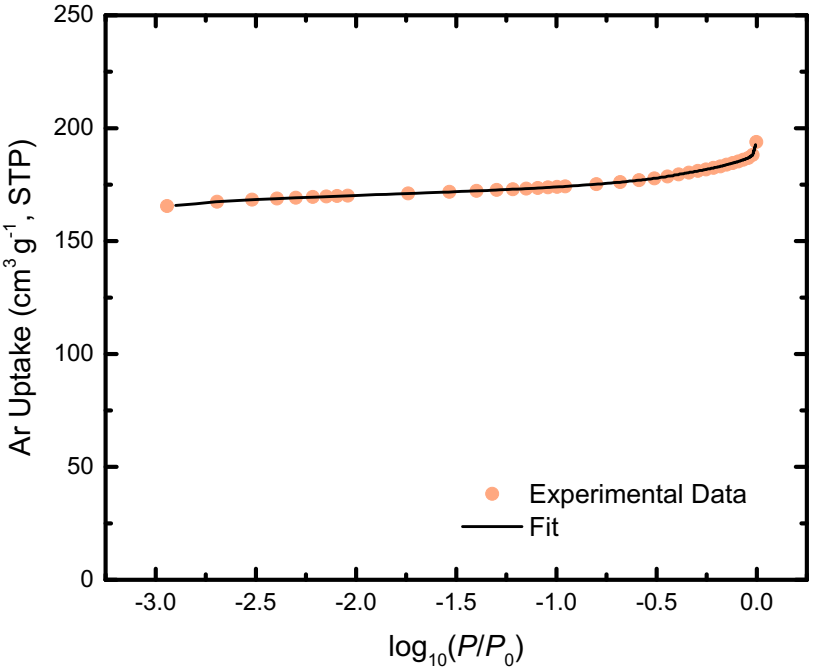

Figure S14. Logarithmic plot of the adsorption branch of the argon sorption isotherm of SAPO-34 at 87 K (*P*: partial pressure of argon, P_0 = 1 atm) and fitting comparison with a NLDFT model (adsorption branch, argon on zeolites at 87 K, spherical/cylindrical pores, fitting error = 0.022%).

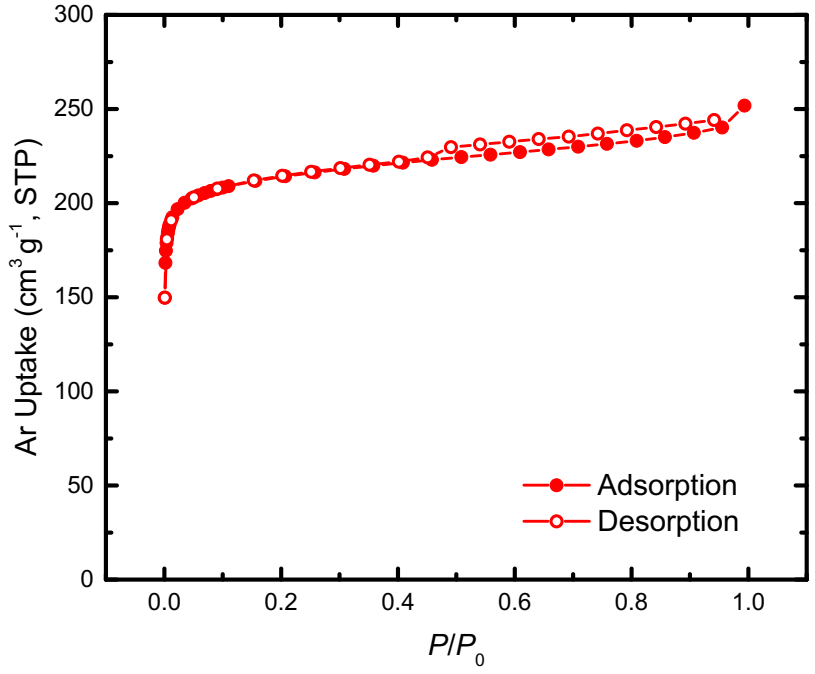

Figure S15. Linear plot of the argon sorption isotherm of zeolite 13X at 87 K (*P*: partial pressure of argon, P_0 = 1 atm). BET surface area: 1077 m^2 g^{-1}.

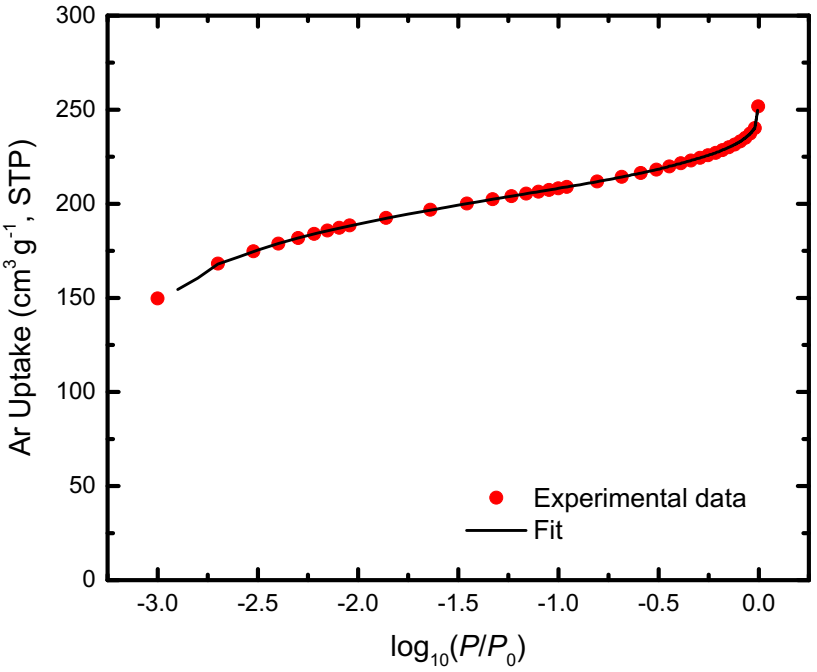

Figure S16. Logarithmic plot of the adsorption branch of the argon sorption isotherm of zeolite 13X at 87 K (*P*: partial pressure of argon, P_0 = 1 atm) and fitting comparison with a NLDFT model (adsorption branch, argon on zeolites at 87 K, cylindrical pores, fitting error = 0.030%).

Section S2.4. Density Determination

After determination of the pore volumes V_{pore} of the sorbent materials through DFT fitting of the argon sorption data, the framework skeletal density ρ_{skel} of all studied adsorbents was measured using a helium (Praxair, ultrahigh purity, 99.999%) pycnometer (Ultrapyc 1200e, Quantachrome). Ten pycnometer measurements were conducted on each material and the average value is reported in Table S1.

The respective powder particle density ρ_p (Table S1) was calculated by the following formula:

$$\rho_p = \frac{1}{\frac{1}{\rho_{skel}} + V_{pore}} \quad \text{(S1)}$$

Table S1. Summary of pore volumes V_{pore}, skeletal densities ρ_{skel} and powder particle densities ρ_p of the sorbents used in this study.

Sorbent	V_{pore} [cm^3 g^{-1}]	ρ_{skel} [g cm^{-3}]	ρ_p [g cm^{-3}]
MOF-303	0.580	1.77	0.873
Al-fumarate	0.574	1.66	0.850
SAPO-34	0.398	2.25	1.19
Zeolite 13X	0.393	2.32	1.21

Section S3. Steady-State Water Sorption Analysis

Volumetric water sorption isotherms were measured on a BEL Japan BELSORP-aqua3. The water (analyte) was degassed through five freeze-pump-thaw cycles before the sorption experiment. Ultrahigh-purity helium (Praxair, 99.999%) was used for dead space estimation.

Section S3.1. Water Sorption Data

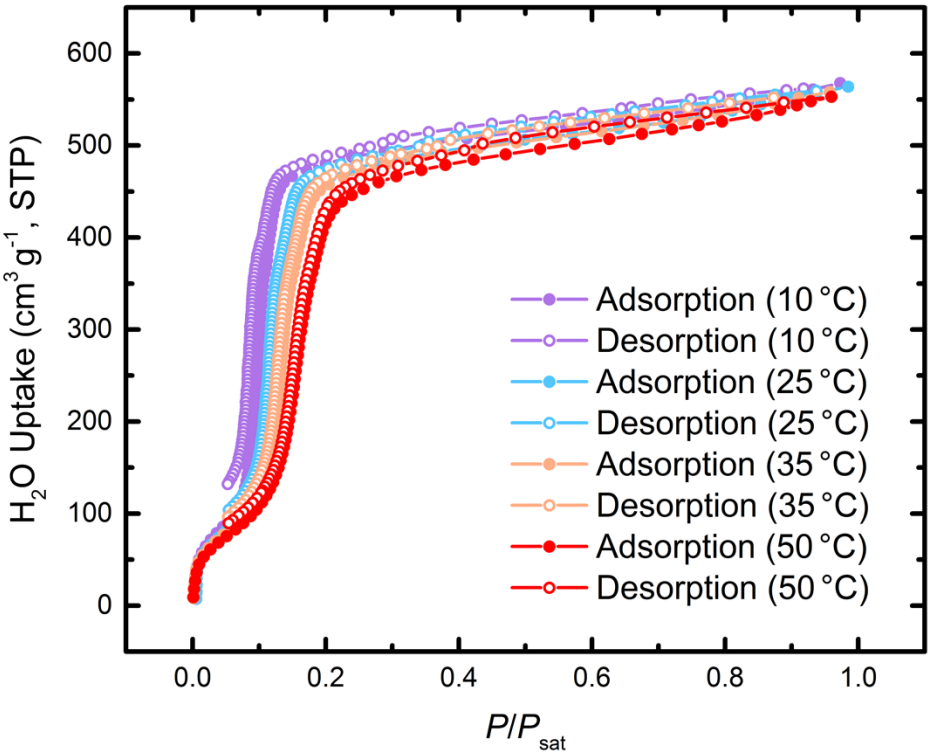

Figure S17. Water vapor uptake of MOF-303 against relative humidity at temperatures between 10 and 50 °C (P: partial water vapor pressure, P_{sat}: saturation water vapor pressure at the given temperature, STP: standard temperature and pressure).

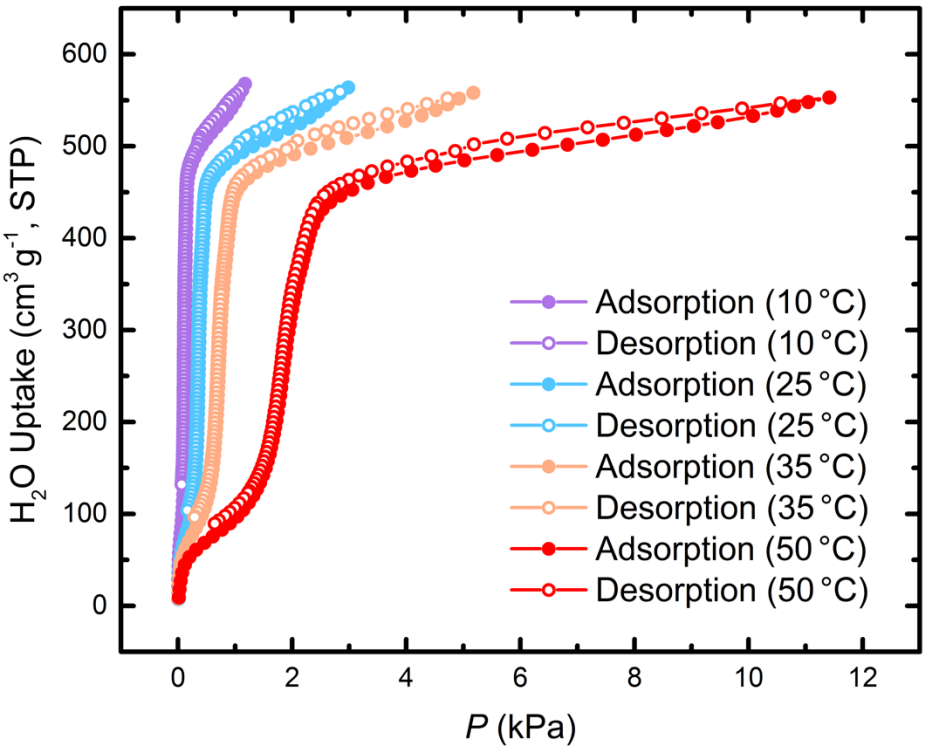

Figure S18. Water vapor uptake of MOF-303 against partial water pressure at temperatures between 10 and 50 °C (*P*: partial water vapor pressure).

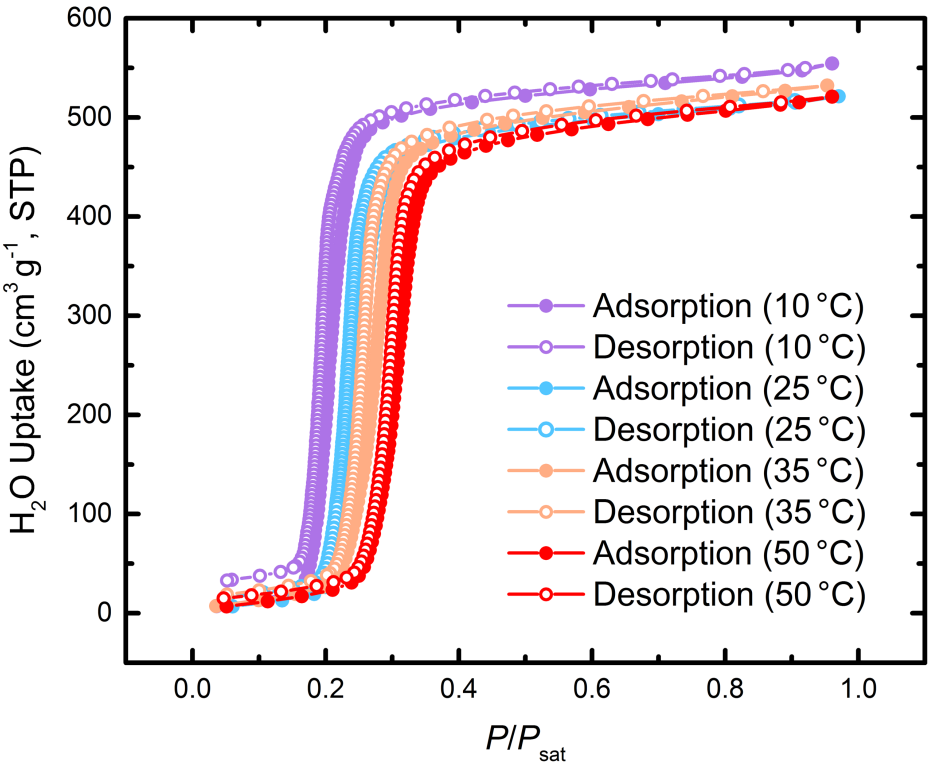

Figure S19. Water vapor uptake of Al-fumarate against relative humidity at temperatures between 10 and 50 °C (*P*: partial water vapor pressure, P_{sat}: saturation water vapor pressure at the given temperature, STP: standard temperature and pressure).

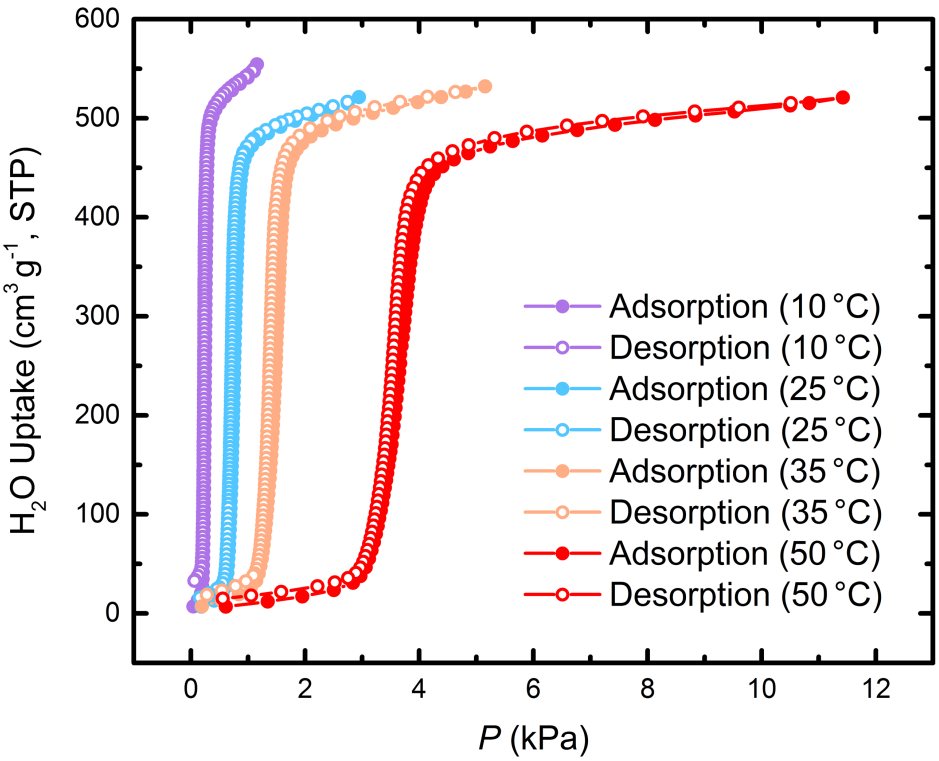

Figure S20. Water vapor uptake of Al-fumarate against partial water pressure at temperatures between 10 and 50 °C (*P*: partial water vapor pressure).

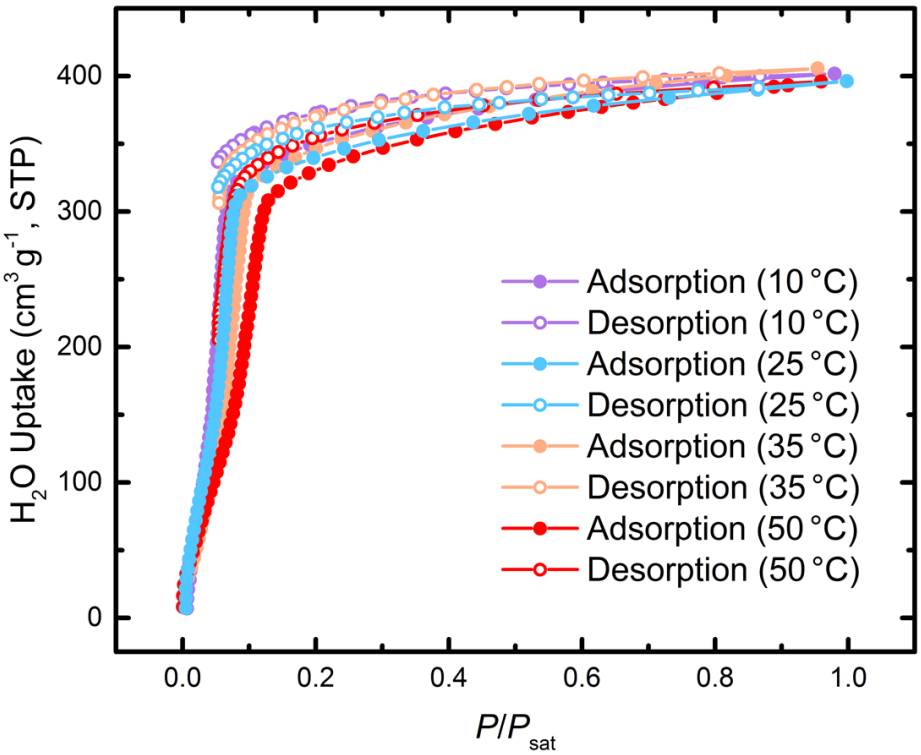

Figure S21. Water vapor uptake of SAPO-34 against relative humidity at temperatures between 10 and 50 °C (*P*: partial water vapor pressure, P_{sat}: saturation water vapor pressure at the given temperature, STP: standard temperature and pressure).

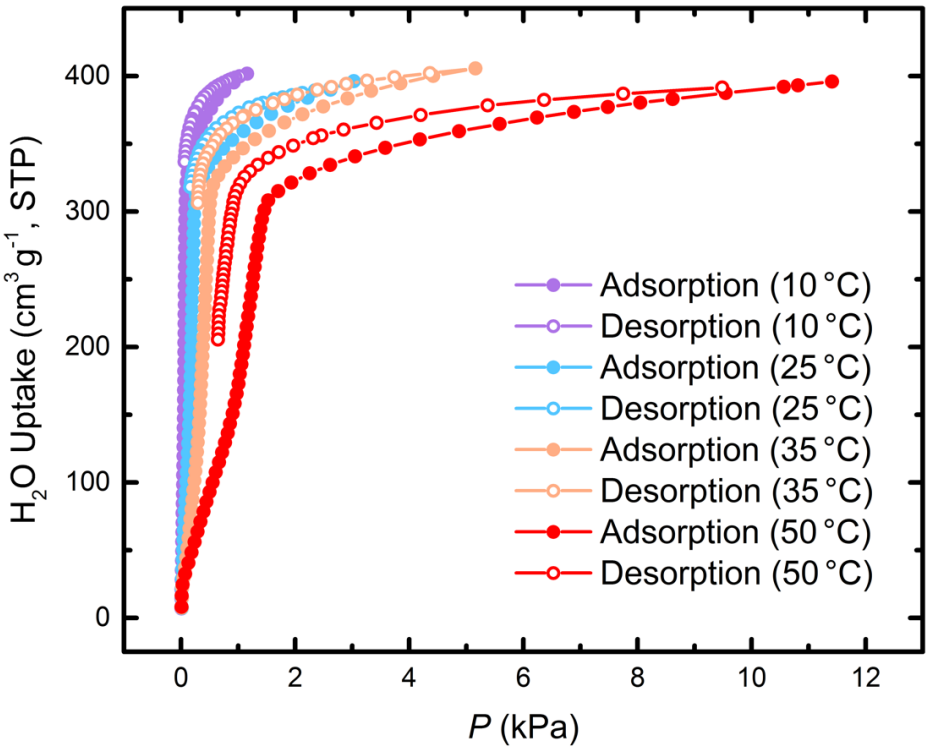

Figure S22. Water vapor uptake of SAPO-34 against partial water pressure at temperatures between 10 and 50 °C (*P*: partial water vapor pressure).

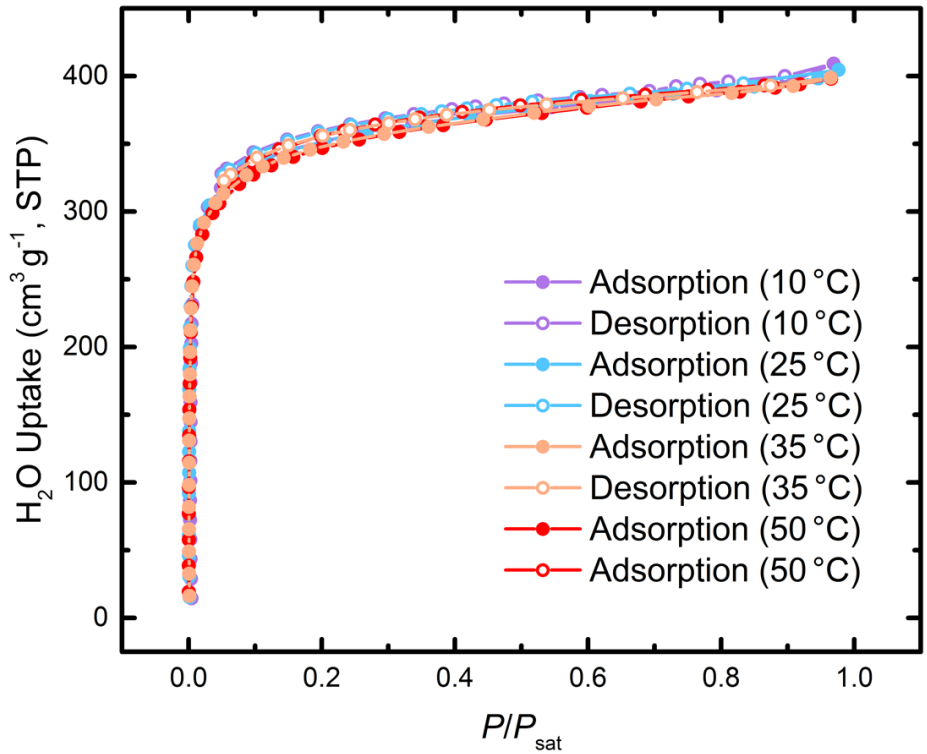

Figure S23. Water vapor uptake of zeolite 13X against relative humidity at temperatures between 10 and 50 °C (*P*: partial water vapor pressure, P_{sat}: saturation water vapor pressure at the given temperature, STP: standard temperature and pressure).

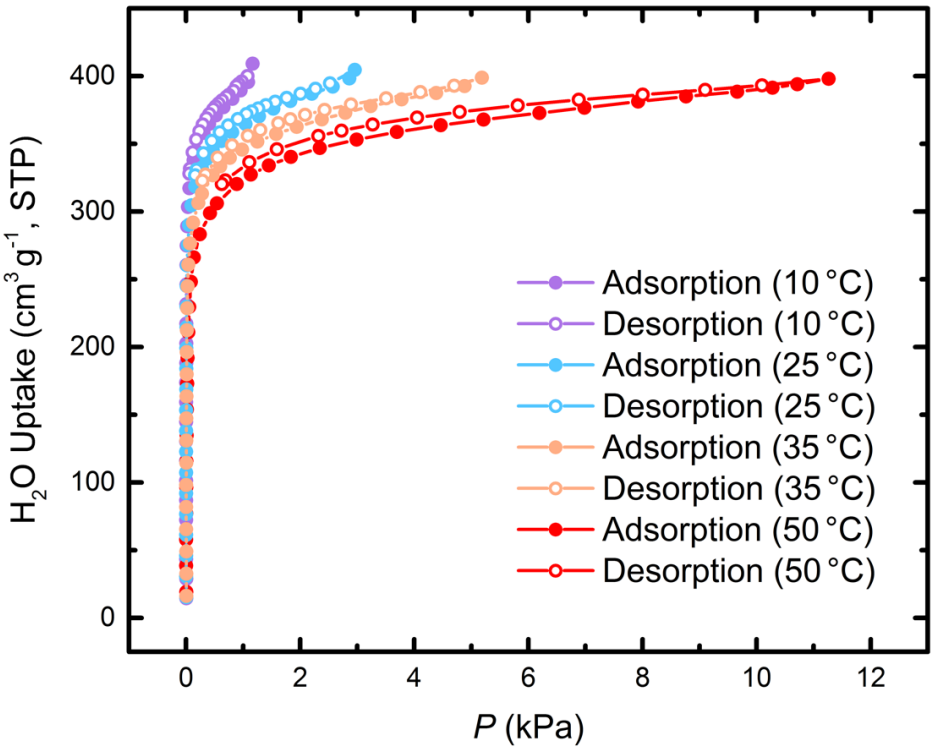

Figure S24. Water vapor uptake of zeolite 13X against partial water pressure at temperatures between 10 and 50 °C (*P*: partial water vapor pressure).

Section S3.2. Estimation of the Isosteric Heats of Adsorption

The isosteric heats of adsorption for MOF-303, Al-fumarate and SAPO-34 were estimated by using the Clausius-Clapeyron relation. This relation could not be used reliably for zeolite 13X, as the separation at low relative vapor pressures between the isotherms at different temperatures is minimal (Figure S23), which is a known limitation of this analysis method.[2]

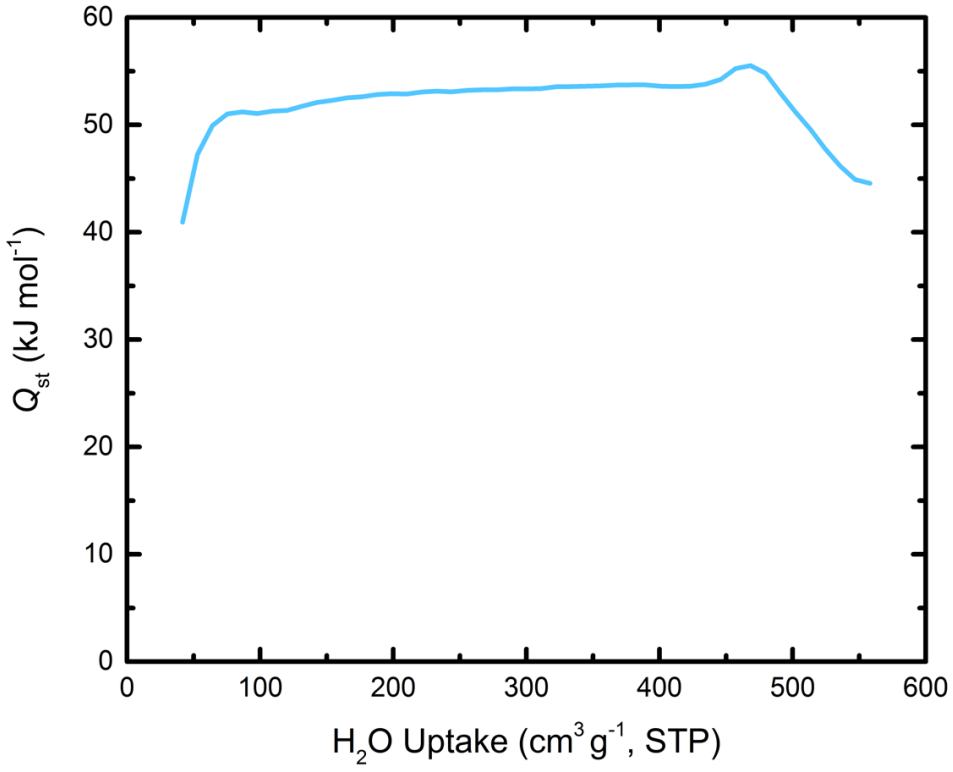

Figure S25. Isosteric heat of adsorption (Q_{st}) in dependence of loading for MOF-303. The Q_{st} was estimated by using water sorption isotherms of MOF-303 at different temperatures (Figure S17).

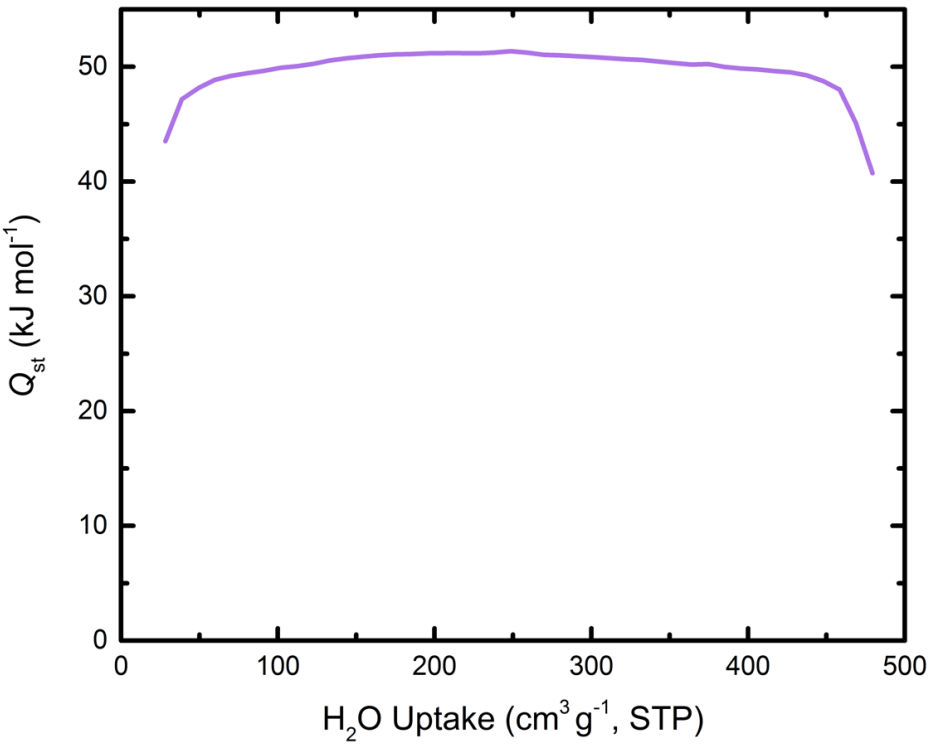

Figure S26. Isosteric heat of adsorption (Q_{st}) in dependence of loading for Al-fumarate. The Q_{st} was estimated by using water sorption isotherms of Al-fumarate at different temperatures (Figure S19).

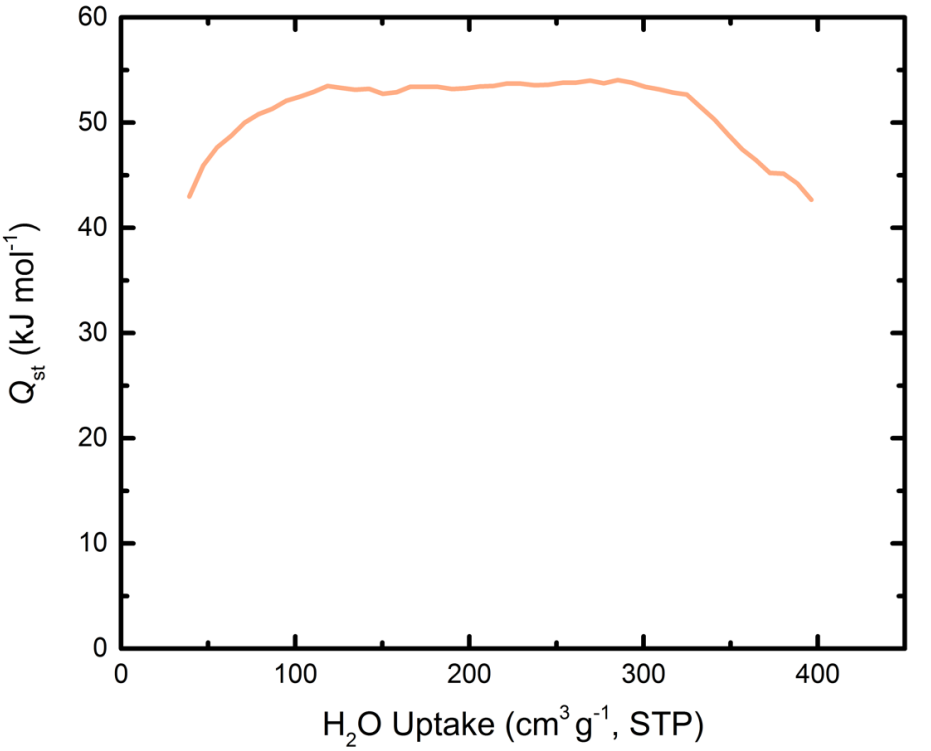

Figure S27. Isosteric heat of adsorption (Q_{st}) in dependence of loading for SAPO-34. The Q_{st} was estimated by using water sorption isotherms of SAPO-34 at different temperatures (Figure S21).

Section S4. Dynamic Water Sorption Analysis

Section S4.1. Calibration of the Setup

For the calibration of the experimental setup described in the Methods Section, the ratio of humidified to dry nitrogen air flow was varied, while the sum of both flows was kept constant at 250 mL min^{-1}. For each data point, the relative humidity (RH) and temperature were recorded.
The measured RH at temperature T (in °C) was corrected with the following temperature compensation relation provided by the sensor manufacturer:

$$\mathrm{RH}(T) = \frac{\mathrm{RH\ (as\ measured)}}{(1.0546 - 0.00216 \cdot T)} \qquad \text{(S2)}$$

The RH at 30 °C (Figure S28) was then calculated based on the Buck equation.[3]

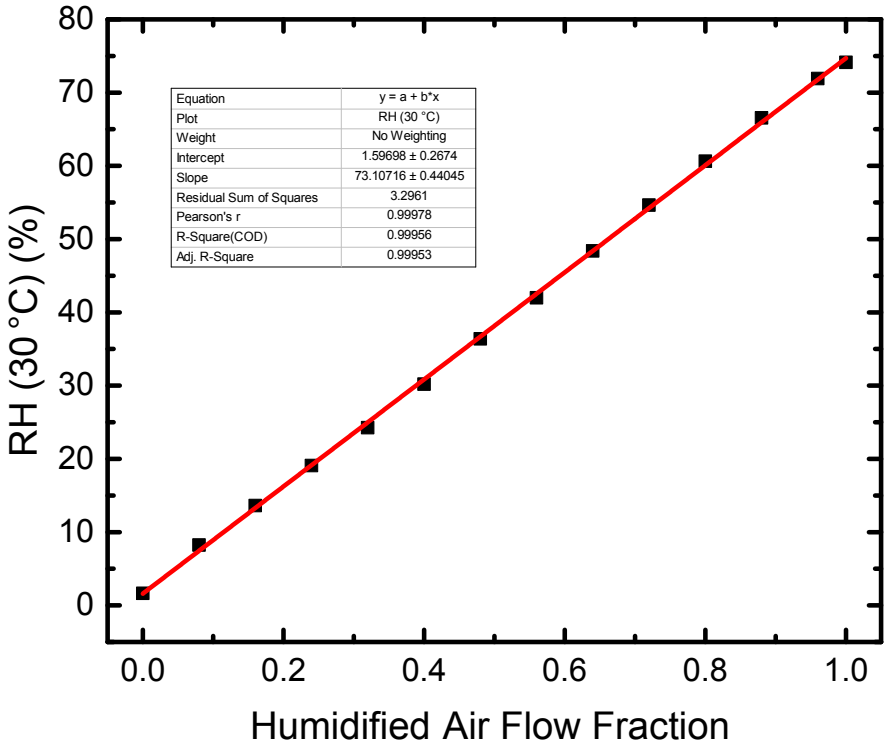

Figure S28. Calibration curve of the thermogravimetric analyzer setup. The generated relative humidity (RH) at 30 °C is plotted against the humidified air flow fraction.

Section S4.2. Flow Characteristics of the Setup

To evaluate the flow characteristics within the TGA setup, the corresponding Reynolds number (at temperatures ranging between 30 and 120 °C) was calculated. The cross-sectional area of the TGA chamber was estimated to be ~4.0 cm^2 (~1.1 cm radius). The flow rate was 250 mL min^{-1} (or 4.17 $cm^3\ s^{-1}$) — resulting in a flow velocity of 1.0 cm s^{-1}.

$$\mathrm{Re} = \frac{V \cdot d_H}{\nu} = \frac{0.010\ \mathrm{m\ s^{-1}} \cdot 0.022\ \mathrm{m}}{2 \cdot 10^{-5} \mathrm{m^2\ s^{-1}}} = 10$$

Thus, the flow within the TGA setup is estimated to be laminar.

Section S4.3. Reproducibility Study

To verify the reproducibility of the dynamic water vapor sorption experiments, duplicate measurements under each experimental condition were conducted. Small deviations within the duplicate measurements can potentially be explained by room temperature deviations (27 ± 0.3 °C), which have an influence on the RH generated by the convective flow through the gas washing bottle filled with water.

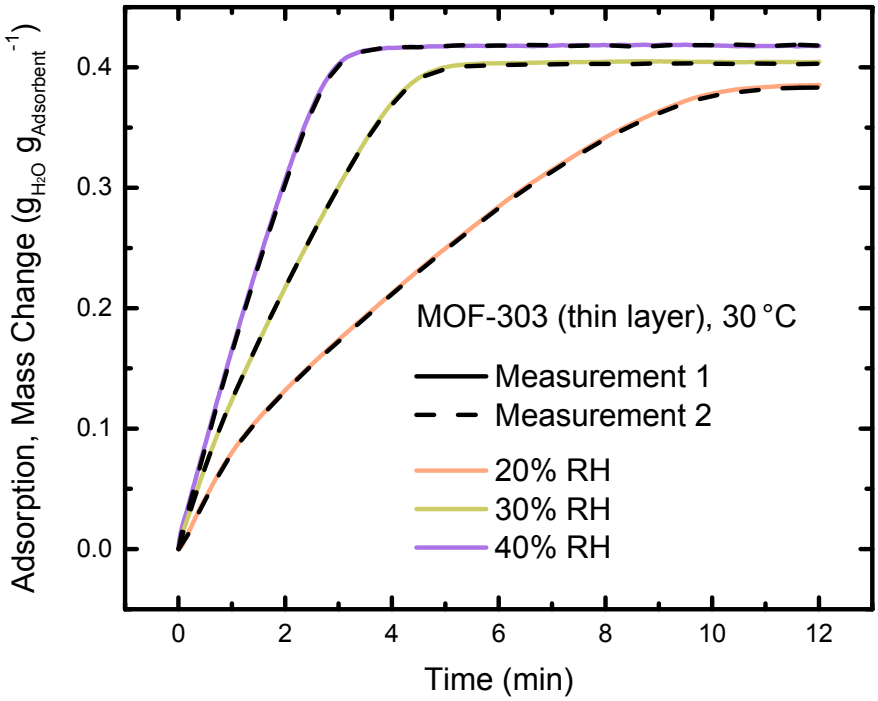

Figure S29. Dynamic water vapor adsorption of a thin layer MOF-303 at 30 °C and relative humidities (RH) ranging between 20 and 40%. Two measurements were conducted at each condition (colored solid and black dashed line). The color of the solid line indicates the corresponding condition.

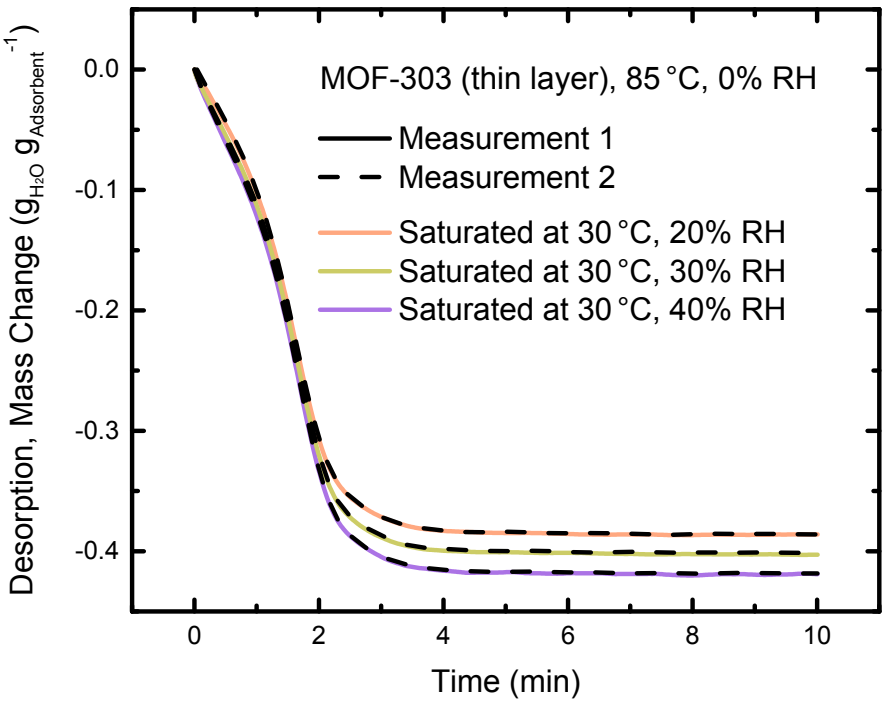

Figure S30. Dynamic water vapor desorption of a thin layer MOF-303 at 85 °C and 0% relative humidity (RH). Prior to desorption, the MOF was saturated at 30 °C and 20-40% RH. Two measurements were conducted at each condition (colored solid and black dashed line). The color of the solid line indicates the corresponding condition.

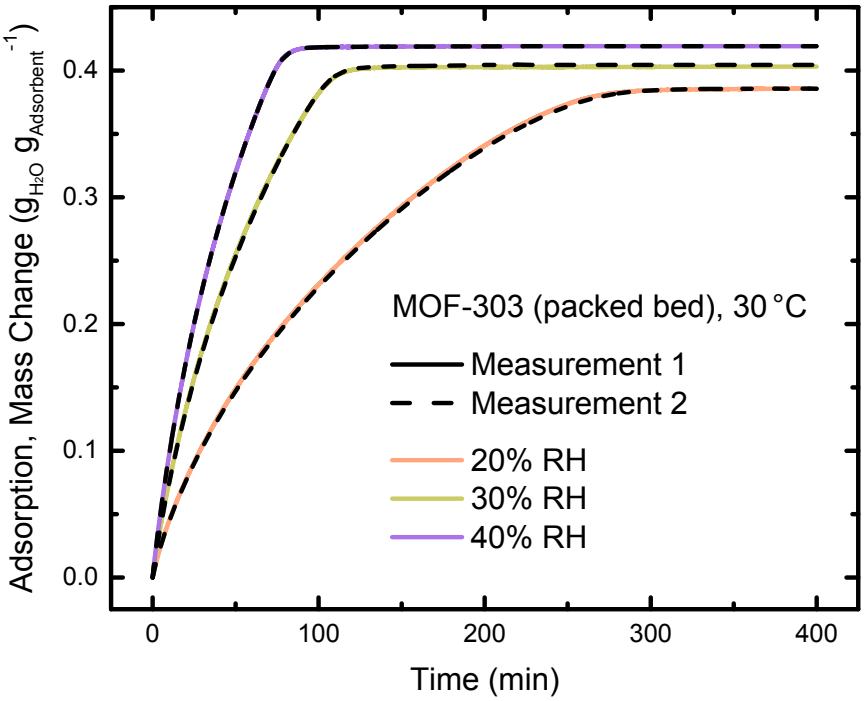

Figure S31. Dynamic water vapor adsorption of MOF-303 in a packed bed configuration at 30 °C and relative humidities (RH) ranging between 20 and 40%. Two measurements were conducted at each condition (colored solid and black dashed line). The color of the solid line indicates the corresponding condition.

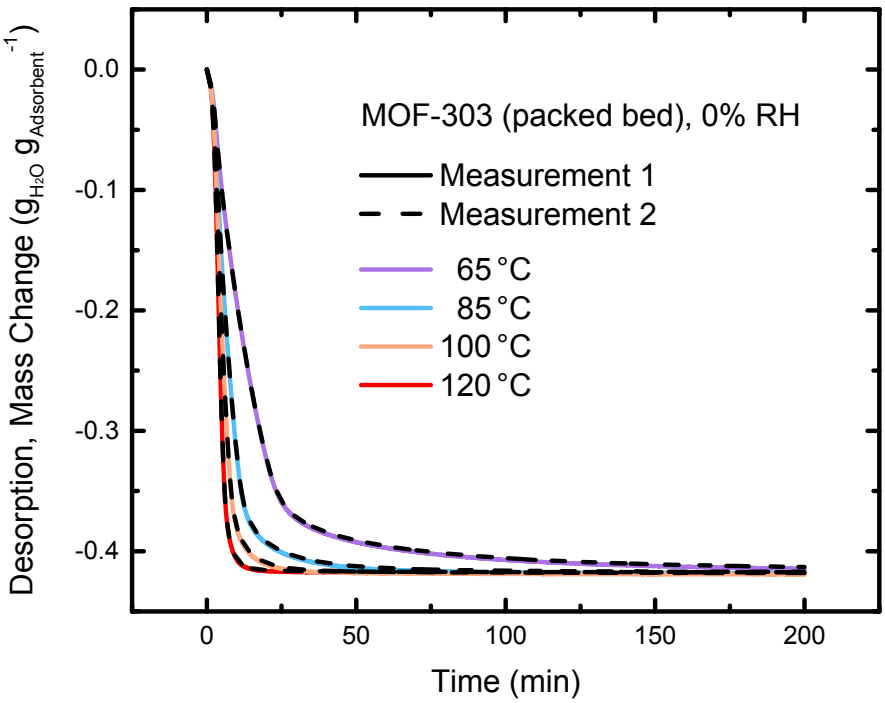

Figure S32. Dynamic water vapor desorption from MOF-303 in a packed bed configuration at temperatures ranging from 65-120 °C and 0% relative humidity (RH). Prior to the measurement, the material was saturated at 30 °C and 40% RH. Two measurements were conducted at each condition (colored solid and black dashed line). The color of the solid line indicates the corresponding condition.

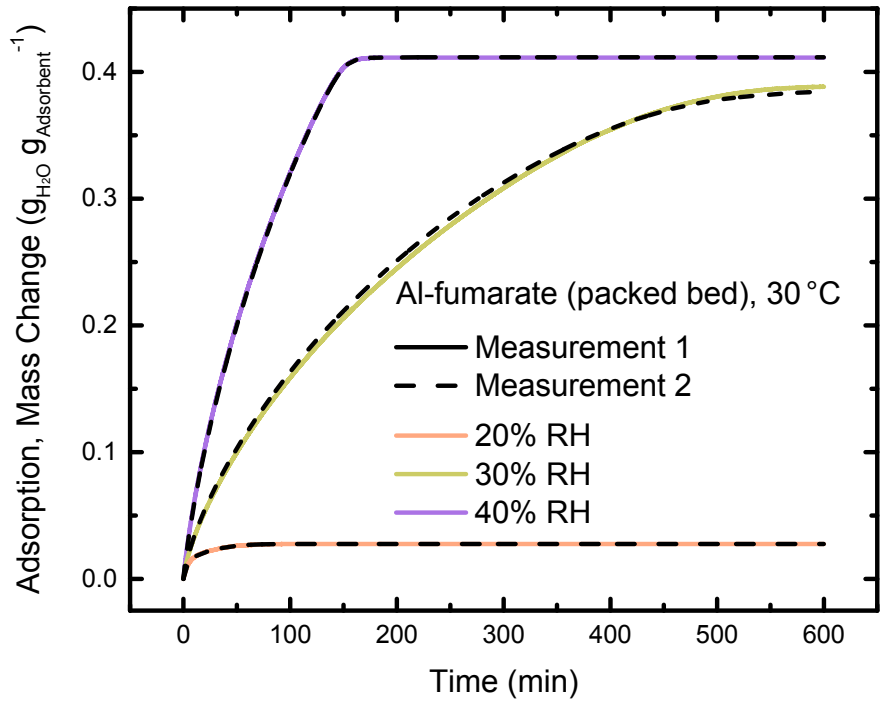

Figure S33. Dynamic water vapor adsorption of Al-fumarate in a packed bed configuration at 30 °C and relative humidities (RH) ranging between 20 and 40%. Two measurements were conducted at each condition (colored solid and black dashed line). The color of the solid line indicates the corresponding condition.

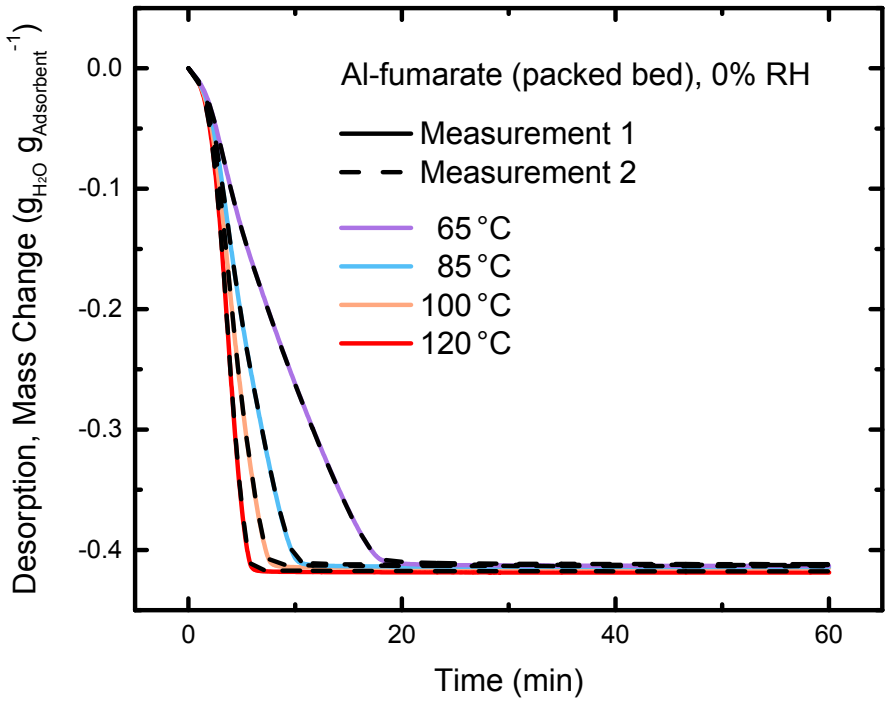

Figure S34. Dynamic water vapor desorption from Al-fumarate in a packed bed configuration at temperatures ranging from 65-120 °C and 0% relative humidity (RH). Prior to the measurement, the material was saturated at 30 °C and 40% RH. Two measurements were conducted at each condition (colored solid and black dashed line). The color of the solid line indicates the corresponding condition.

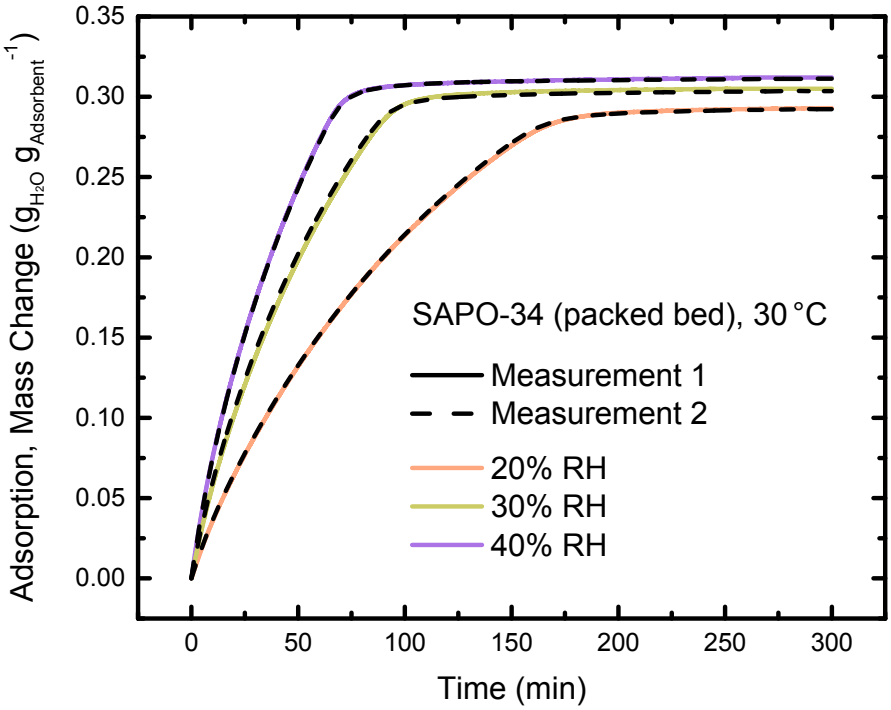

Figure S35. Dynamic water vapor adsorption of SAPO-34 in a packed bed configuration at 30 °C and relative humidities (RH) ranging between 20 and 40%. Two measurements were conducted at each condition (colored solid and black dashed line). The color of the solid line indicates the corresponding condition.

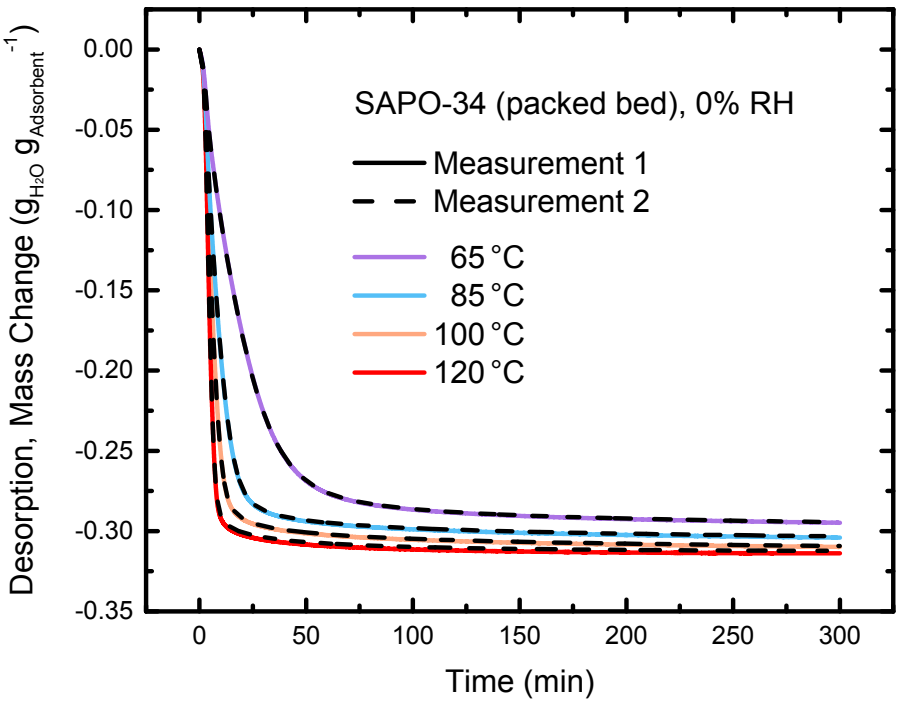

Figure S36. Dynamic water vapor desorption from SAPO-34 at temperatures ranging from 65-120 °C and 0% relative humidity (RH). Prior to the measurement, the material was saturated at 30 °C and 40% RH. Two measurements were conducted at each condition (colored solid and black dashed line). The color of the solid line indicates the corresponding condition.

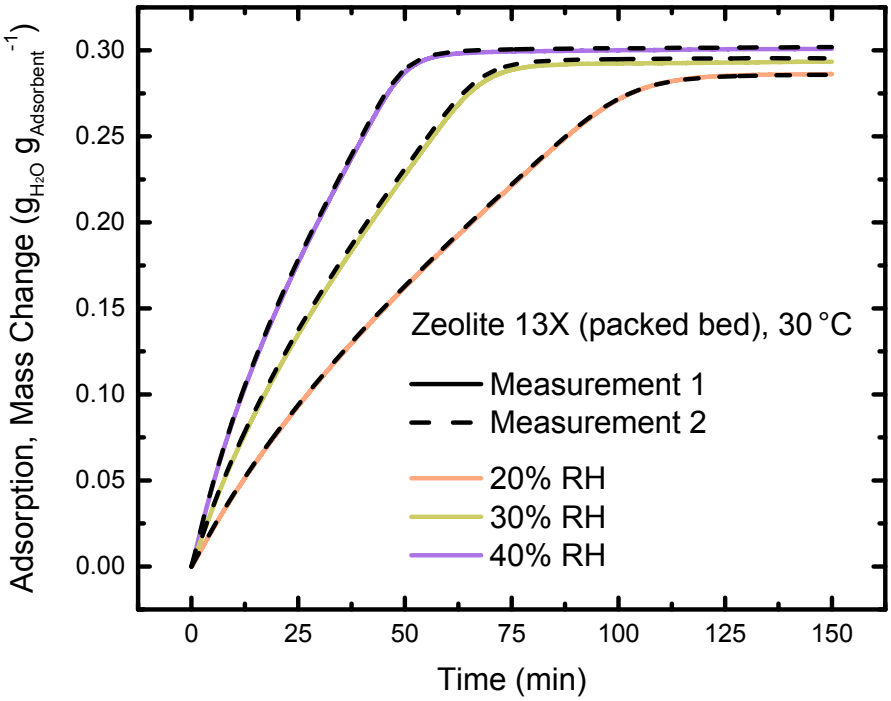

Figure S37. Dynamic water vapor adsorption of zeolite 13X in a packed bed configuration at 30 °C and relative humidities (RH) ranging between 20 and 40%. Two measurements were conducted at each condition (colored solid and black dashed line). The color of the solid line indicates the corresponding condition.

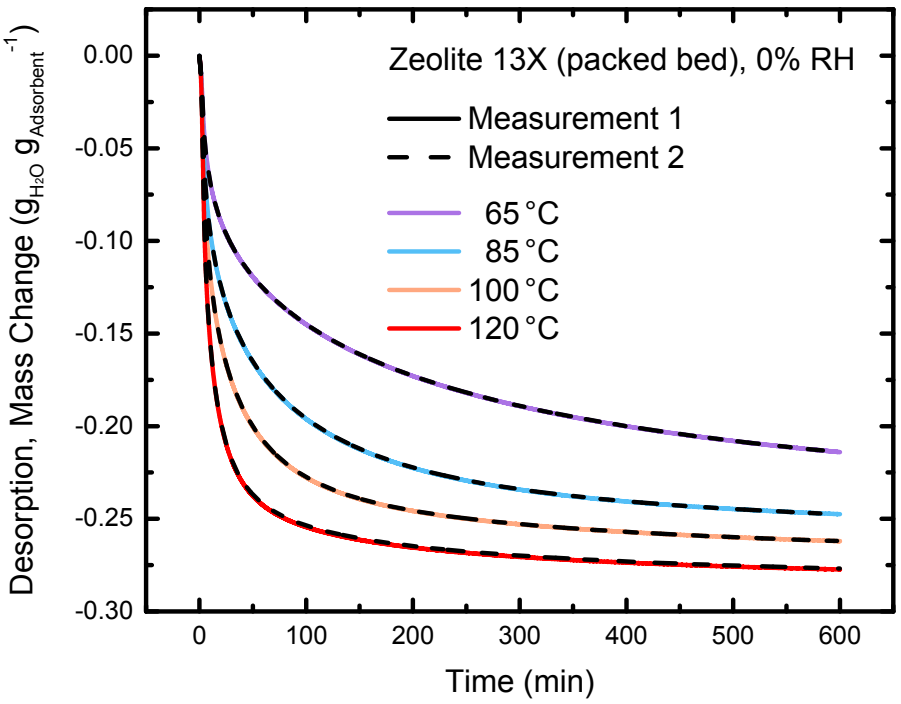

Figure S38. Dynamic water vapor desorption from zeolite 13X in a packed bed configuration at temperatures ranging from 65-120 °C and 0% relative humidity (RH). Prior to the measurement, the material was saturated at 30 °C and 40% RH. Two measurements were conducted at each condition (colored solid and black dashed line). The color of the solid line indicates the corresponding condition.

Section S4.4. Fitting the Experimental Dynamic Adsorption Data

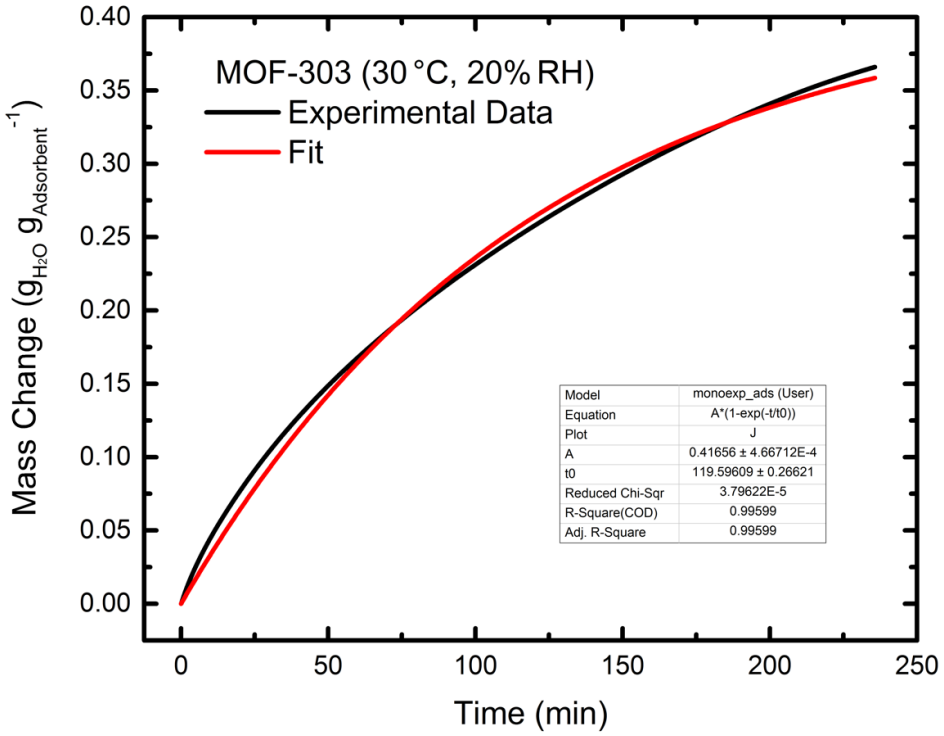

Figure S39. Mono-exponential approximation of the dynamic water adsorption process in MOF-303 at 30 °C and 20% relative humidity (RH).

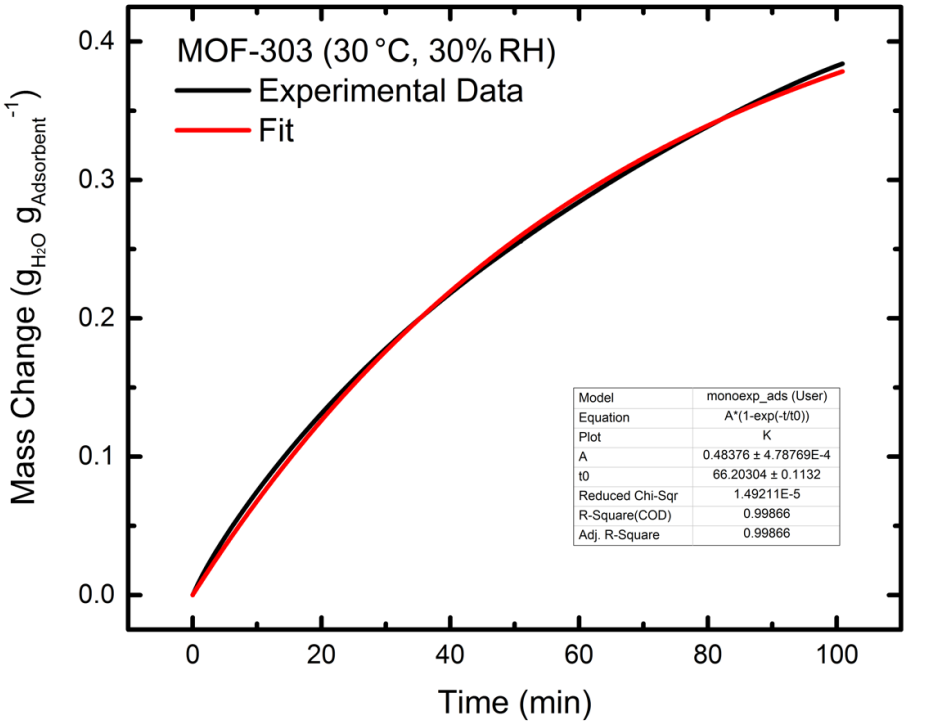

Figure S40. Mono-exponential approximation of the dynamic water adsorption process in MOF-303 at 30 °C and 30% relative humidity (RH).

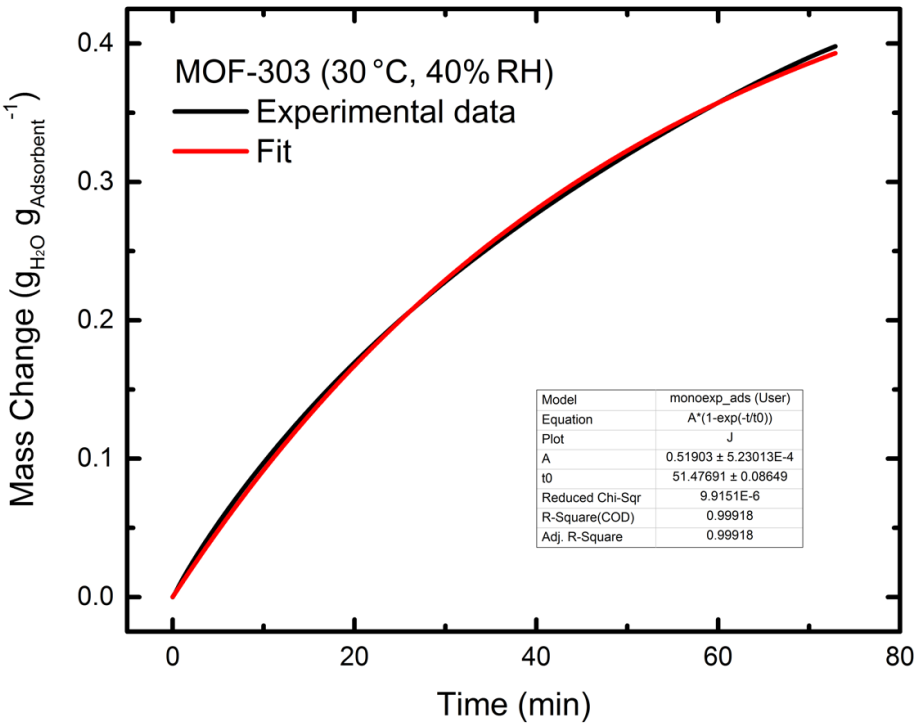

Figure S41. Mono-exponential approximation of the dynamic water adsorption process in MOF-303 at 30 °C and 40% relative humidity (RH).

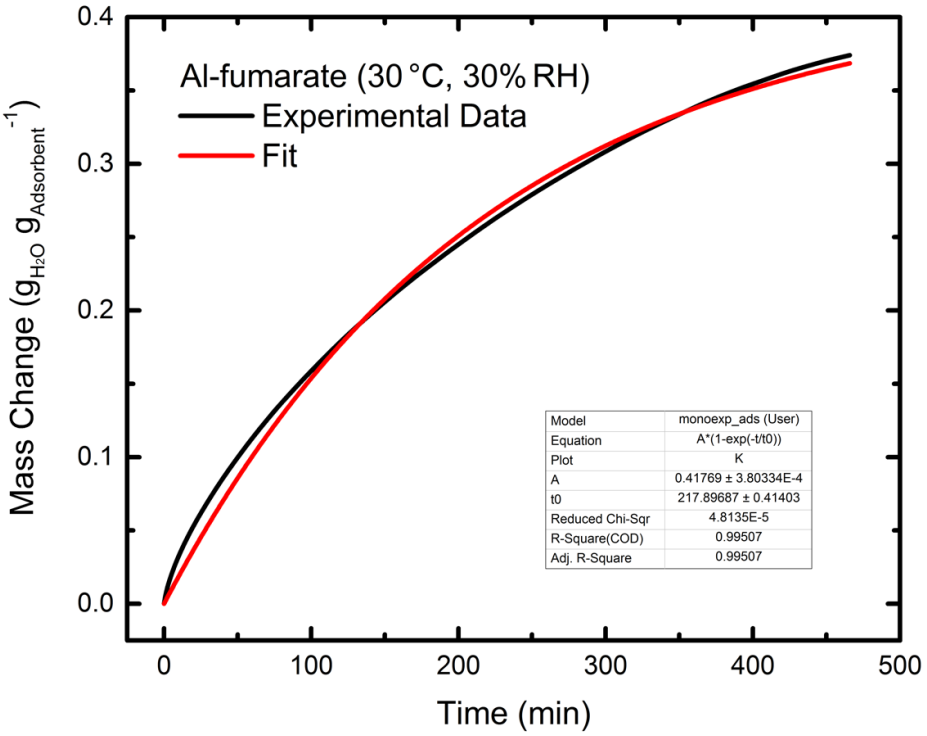

Figure S42. Mono-exponential approximation of the dynamic water adsorption process in Al-fumarate at 30 °C and 30% relative humidity (RH).

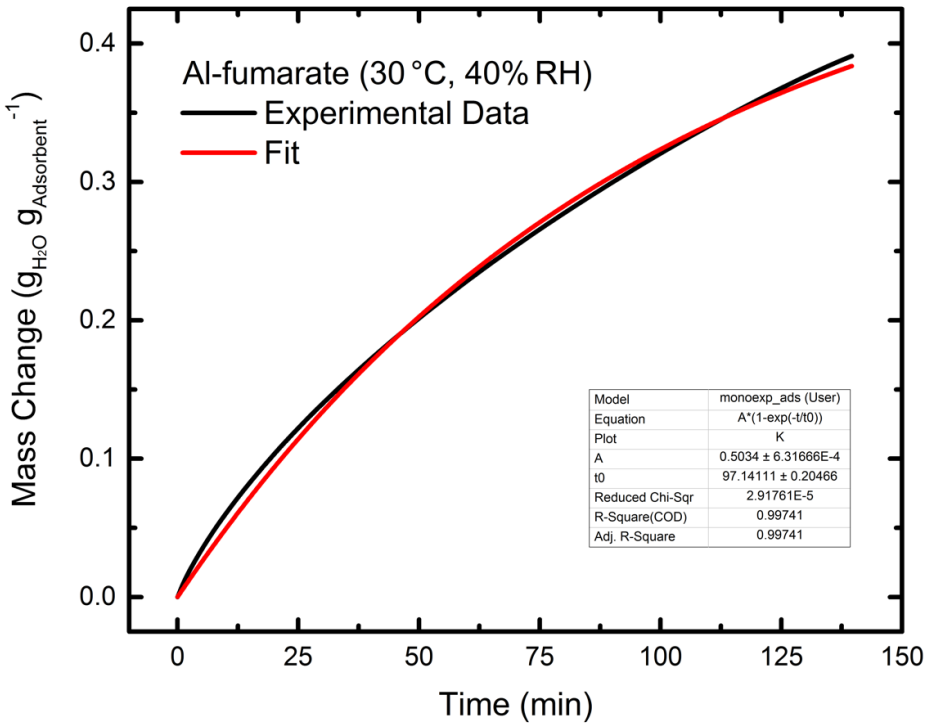

Figure S43. Mono-exponential approximation of the dynamic water adsorption process in Al-fumarate at 30 °C and 40% relative humidity (RH).

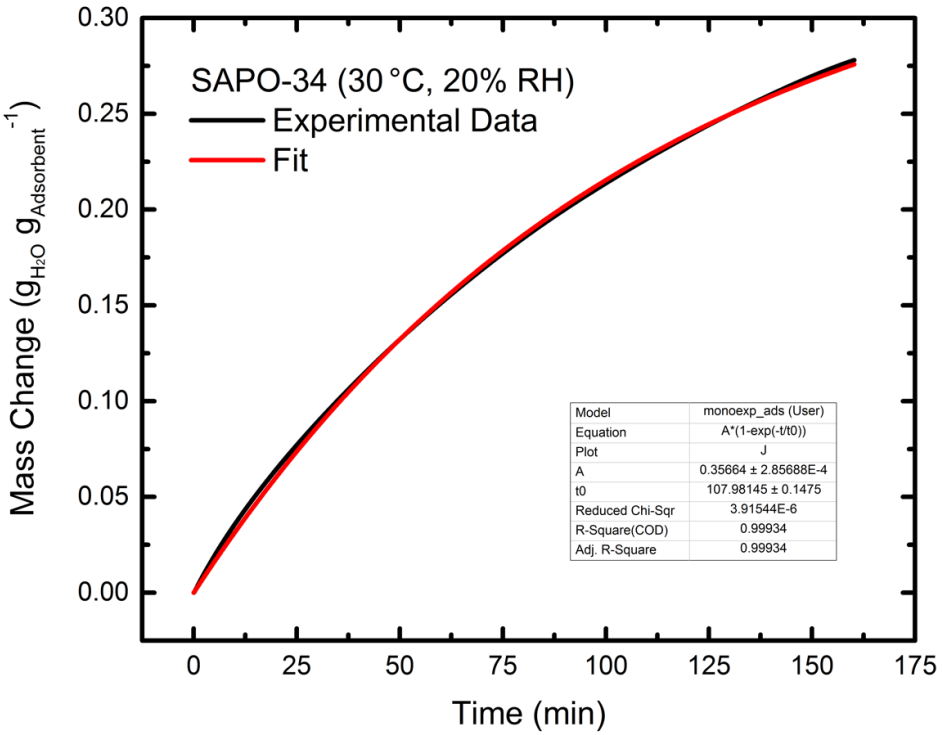

Figure S44. Mono-exponential approximation of the dynamic water adsorption process in SAPO-34 at 30 °C and 20% relative humidity (RH).

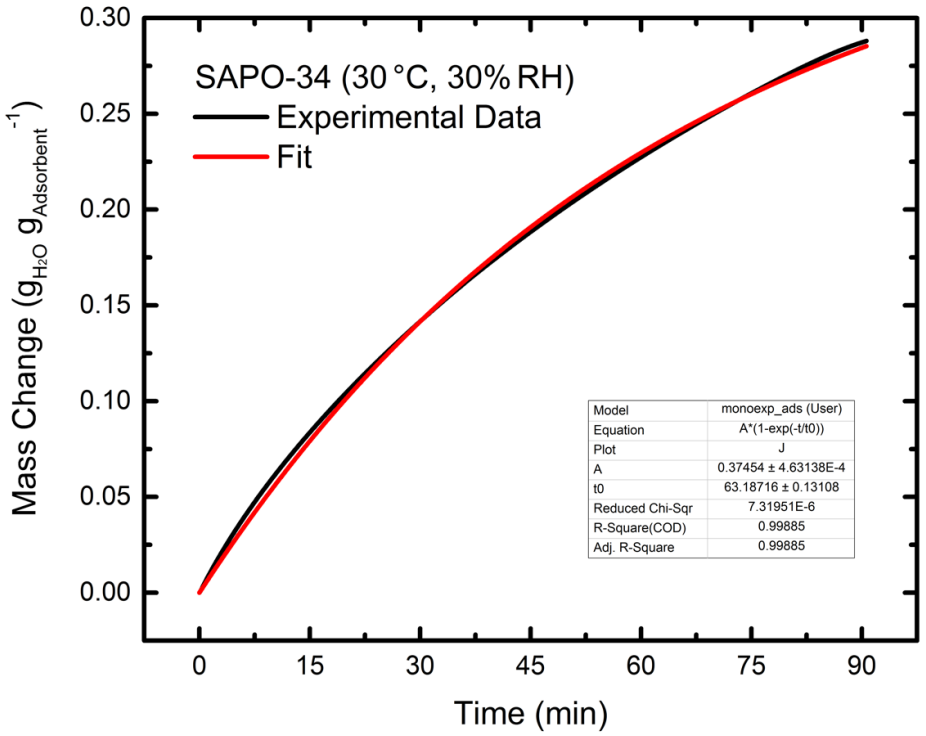

Figure S45. Mono-exponential approximation of the dynamic water adsorption process in SAPO-34 at 30 °C and 30% relative humidity (RH).

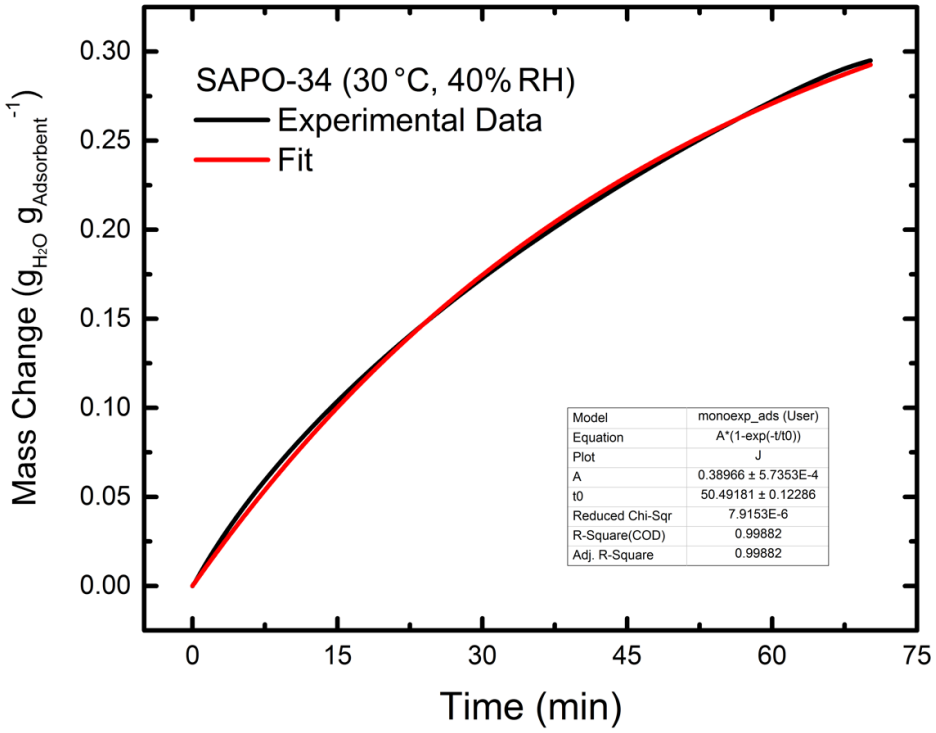

Figure S46. Mono-exponential approximation of the dynamic water adsorption process in SAPO-34 at 30 °C and 40% relative humidity (RH).

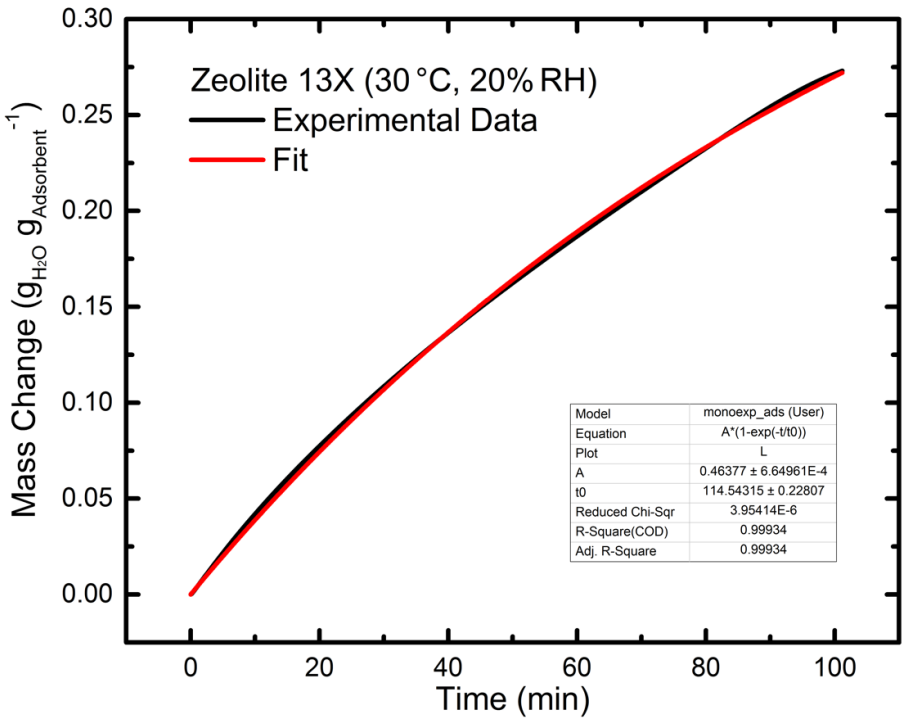

Figure S47. Mono-exponential approximation of the dynamic water adsorption process in zeolite 13X at 30 °C and 20% relative humidity (RH).

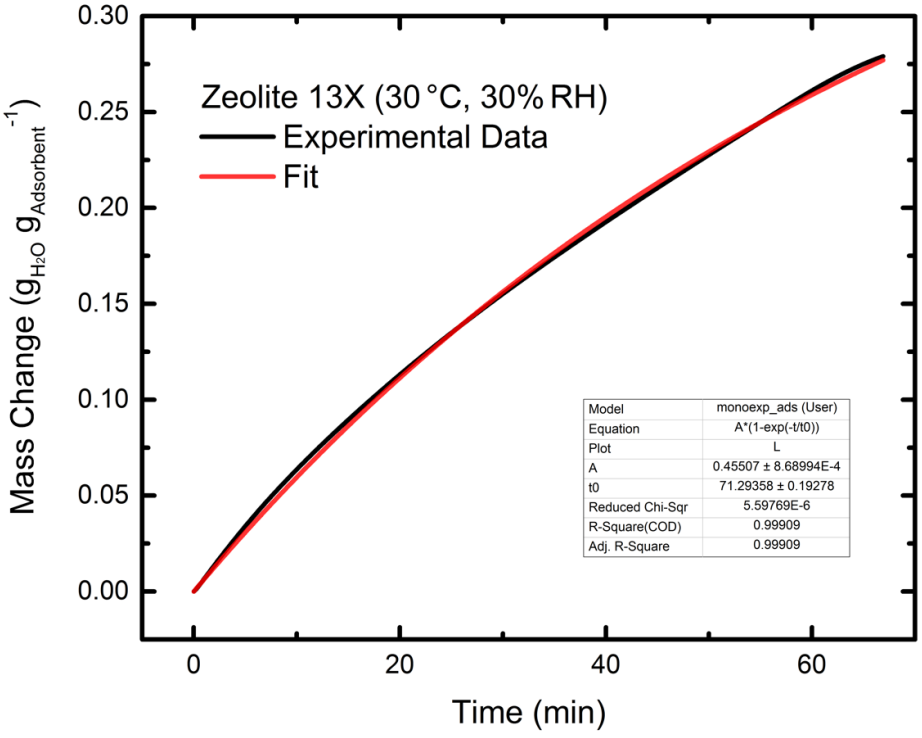

Figure S48. Mono-exponential approximation of the dynamic water adsorption process in zeolite 13X at 30 °C and 30% relative humidity (RH).

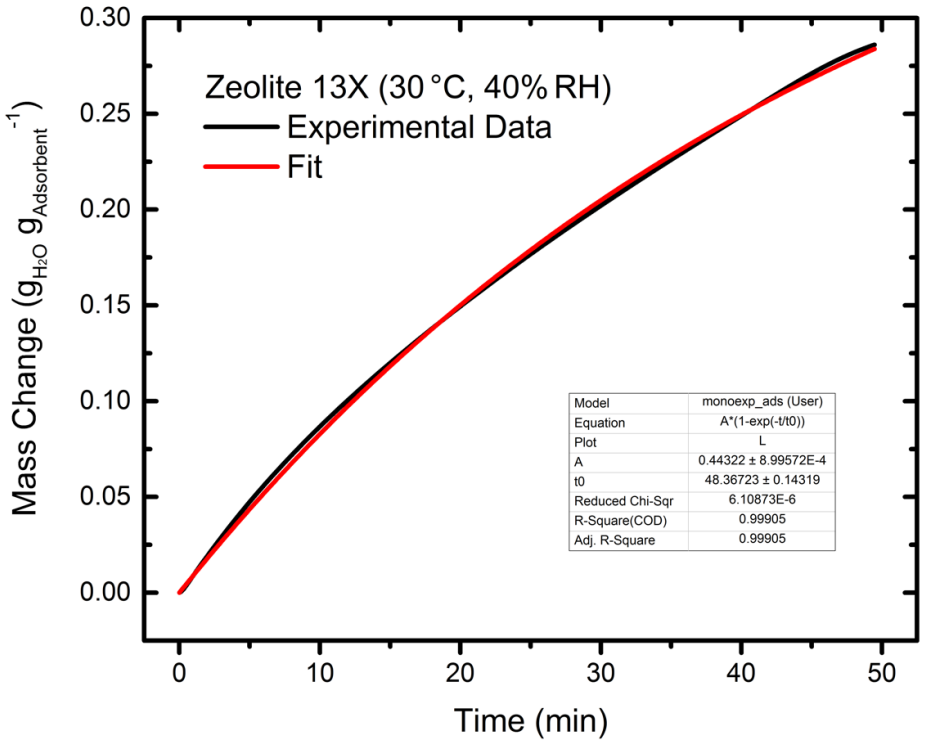

Figure S49. Mono-exponential approximation of the dynamic water adsorption process in zeolite 13X at 30 °C and 40% relative humidity (RH).

Section S5. Cross-flow exchanger assembly

Section S5.1. Exchanger assembly

The sorbent-containing exchanger was prepared in several steps. First, a removable cartridge, containing the sorbent powder was built according to the following procedure (Figure S50): Ten frames (dimensions: $9.75 \times 9.75 \times 0.25$ in^3), exhibiting four empty square areas each (of dimensions $4.5 \times 4.5 \times 0.25$ in^3) and made of carbon-fiber-reinforced ONYX, were 3D-printed using a Markforged Mark X7 printer (see Figure S51 for a blueprint of a frame). Subsequently, the frames were lined on one side with a PTFE laminated membrane (pore size 0.45 µm, Sterlitech Corporation) using Gorilla Super Glue, followed by drying overnight. Microporous PTFE was chosen because of its ability to repel liquid water while allowing for efficient water vapor transport.[4] Then, 433 g of fully desorbed sorbent powder (MOF-303 or Al-fumarate) were distributed evenly inside of the empty spaces of the frames, forming 40 sorbent beds, which were subsequently enclosed with another PTFE membrane glued on the other side of the frame. The glue was again left to dry overnight. The filled trays were finally assembled into a cartridge using acrylic spacers (Figure S51) and Gorilla Super Glue. The final cartridge exhibited two sets of 0.25 in-wide orthogonal channels, allowing for convection from and towards the sorbent powder (Figure S51). Once again, the glue was let to dry overnight, using C-clamps to apply pressure and ensure adequate contact between the different parts. The sorbent cartridge was then wrapped with four heating strips (1 in × 96 in, 120 V, 830 W, BriskHeat B00101080), and installed inside of a custom-made acrylic enclosure (dimensions: $23.2 \times 12.6 \times 15.25$ in^3, Figure S52-S55). This enclosure was equipped with one fan (12 V, 0.3 A, Sunon MF40101VX-1000U-A99) for convective mass transfer during the water adsorption phase, using one set of channels, and eight smaller fans (5VDC, 3.3 CFM, Qualtek FAD1-04010BSAW11) for forced convection of the generated vapor during the desorption phase, using the other set of channels (Figure S52).

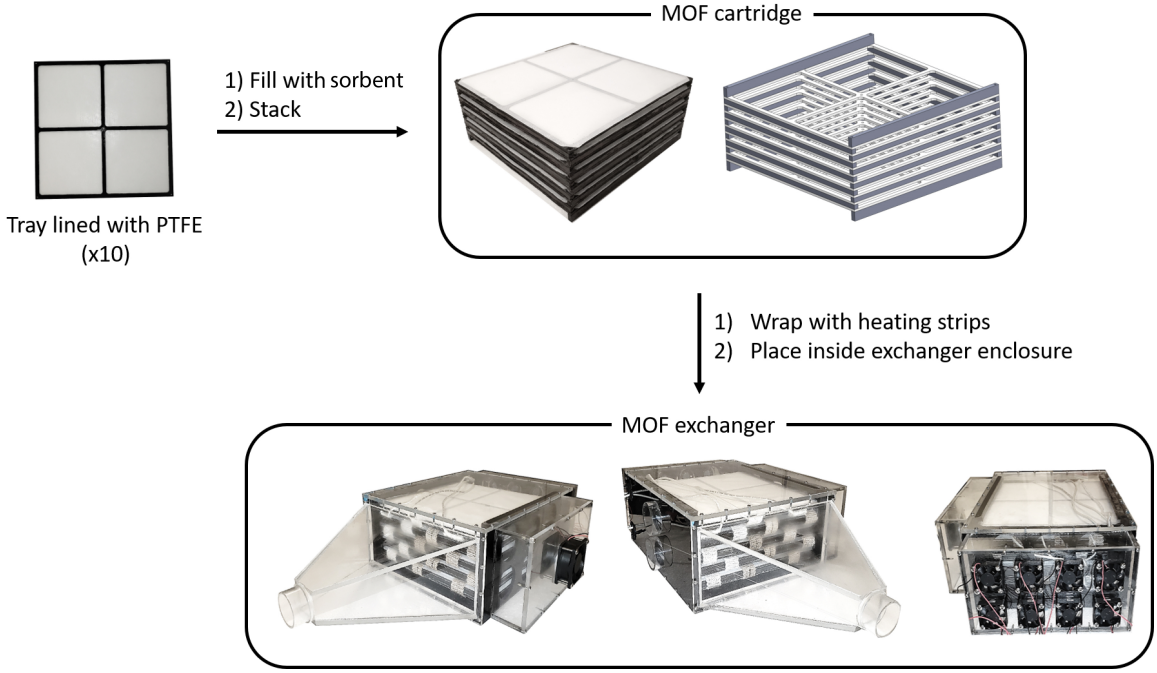

Figure S50. General scheme describing the assembly steps for the sorbent exchanger.

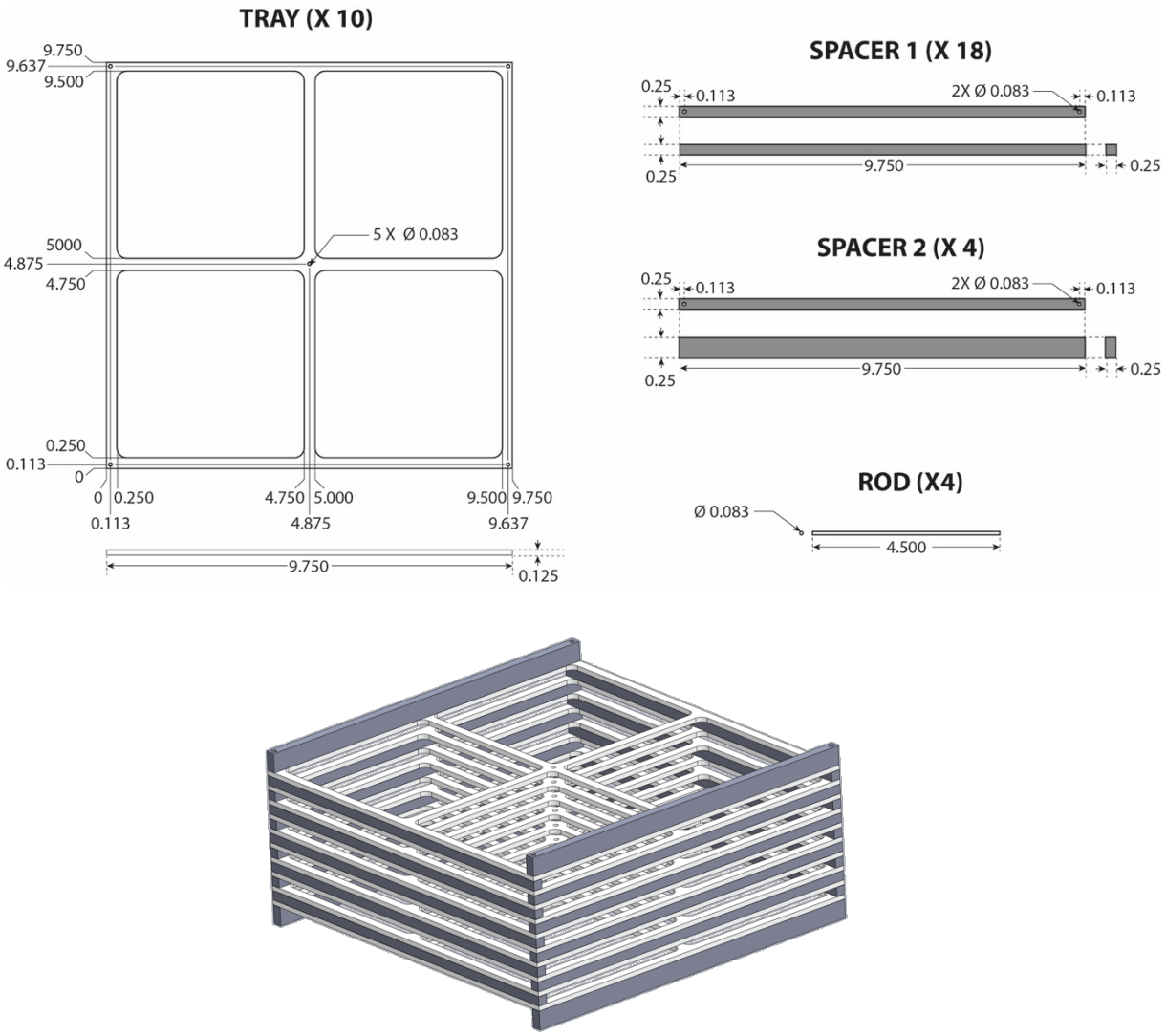

Figure S51. Blueprints of the component of the sorbent cartridge, and illustration of the assembled cartridge containing 10 trays, 18 thin spacers, 4 wide spacers and 4 rods to hold the cartridge together. The PTFE membranes lining the tray and the sorbent powder they contain are omitted for clarity. All distances are in inches.

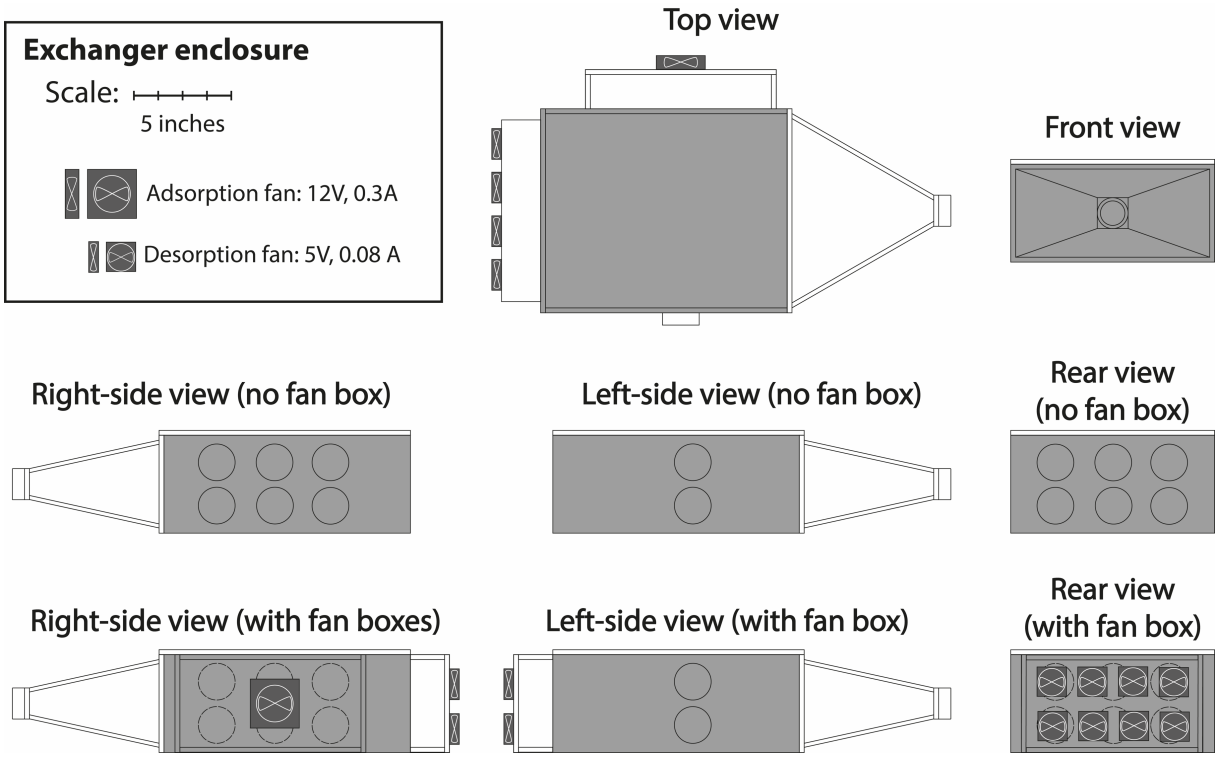

Figure S52. Illustration of the exchanger enclosure designed to host the sorbent cartridge, with and without the fan boxes used to equip the enclosure with the fans generating convective air flow during operation.

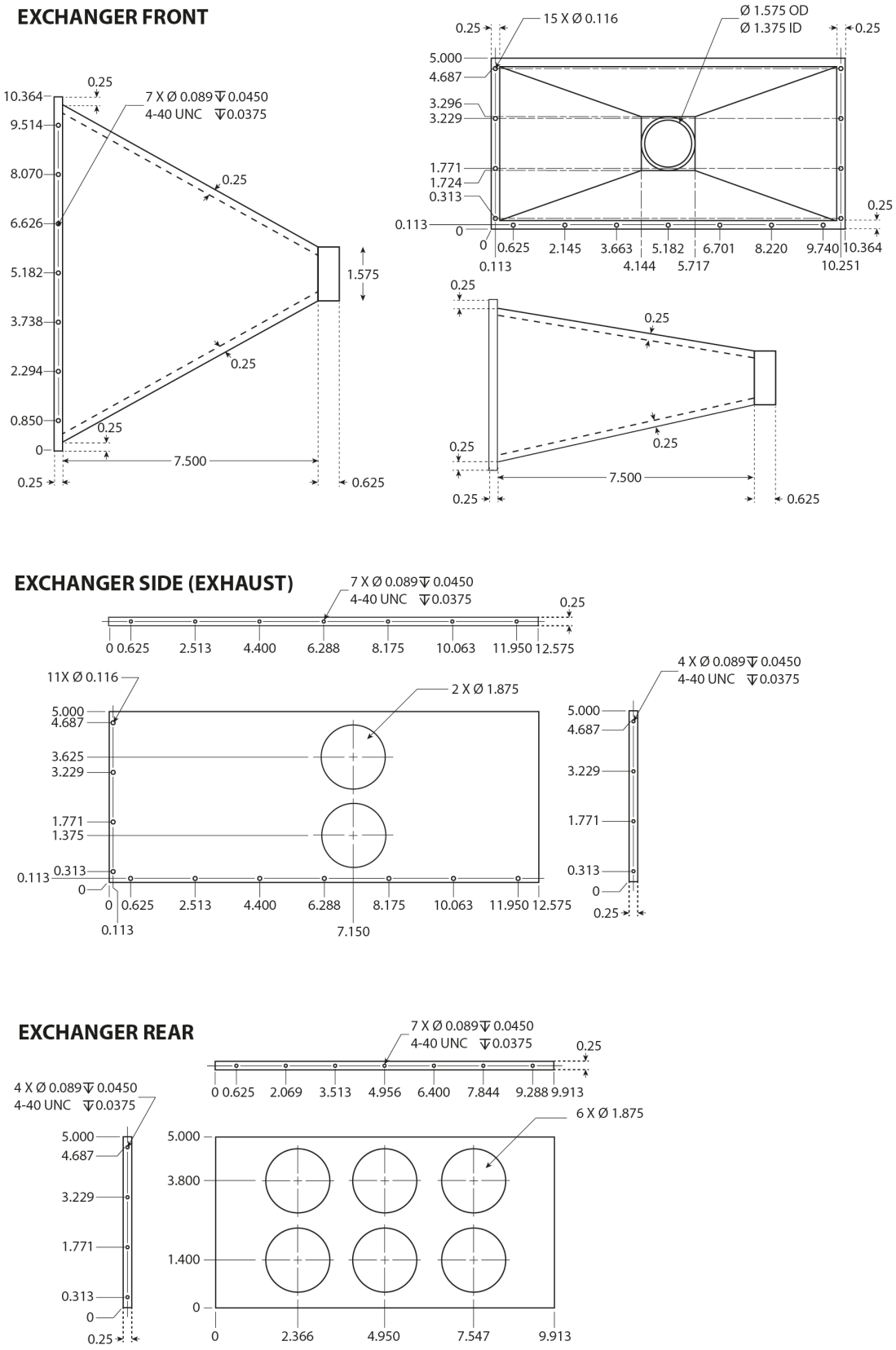

Figure S53. Blueprints of the exchanger front, exhaust side and rear. All distances are in inches.

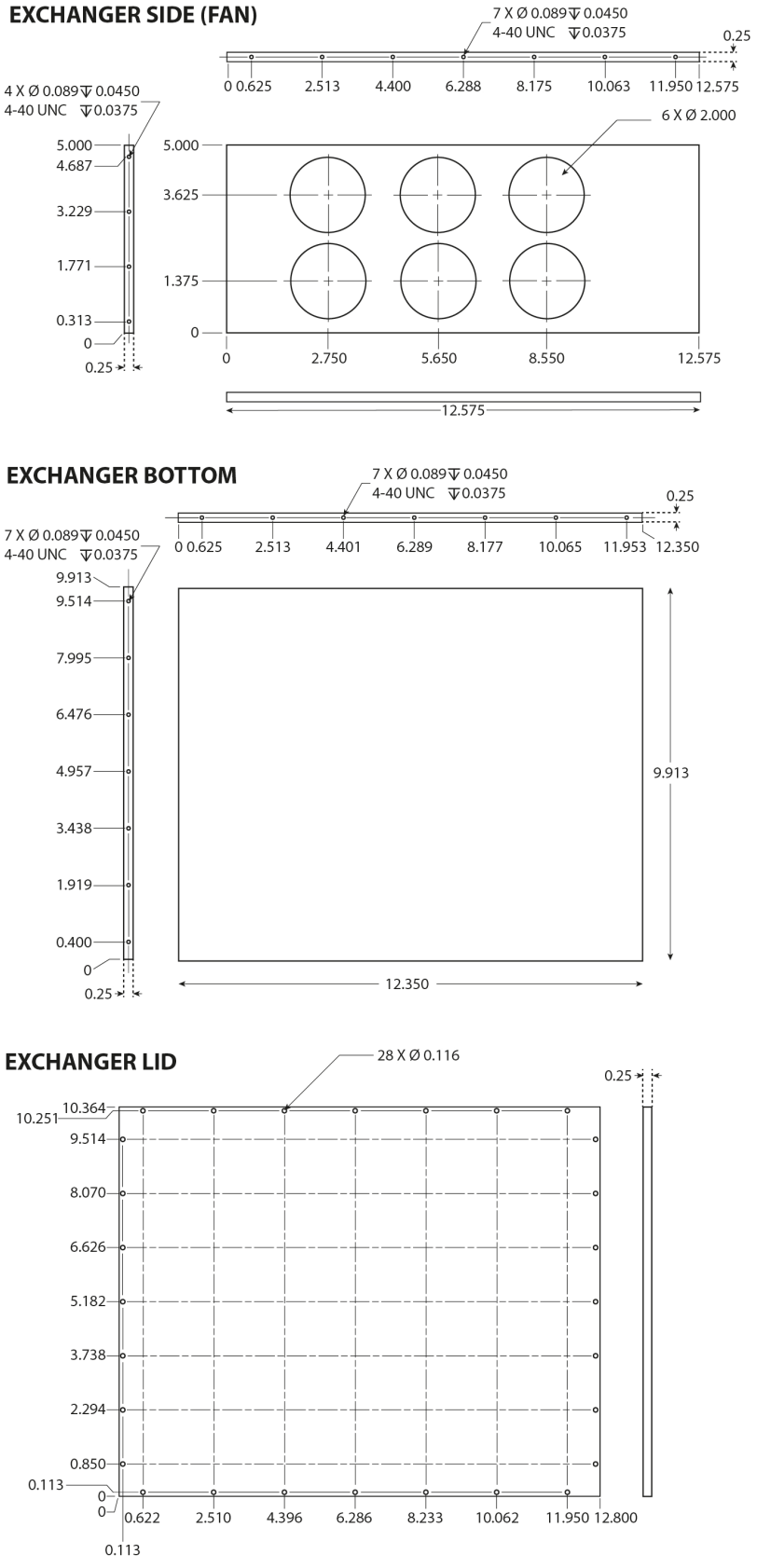

Figure S54. Blueprints of the exchanger fan side, bottom and lid. All distances are in inches.

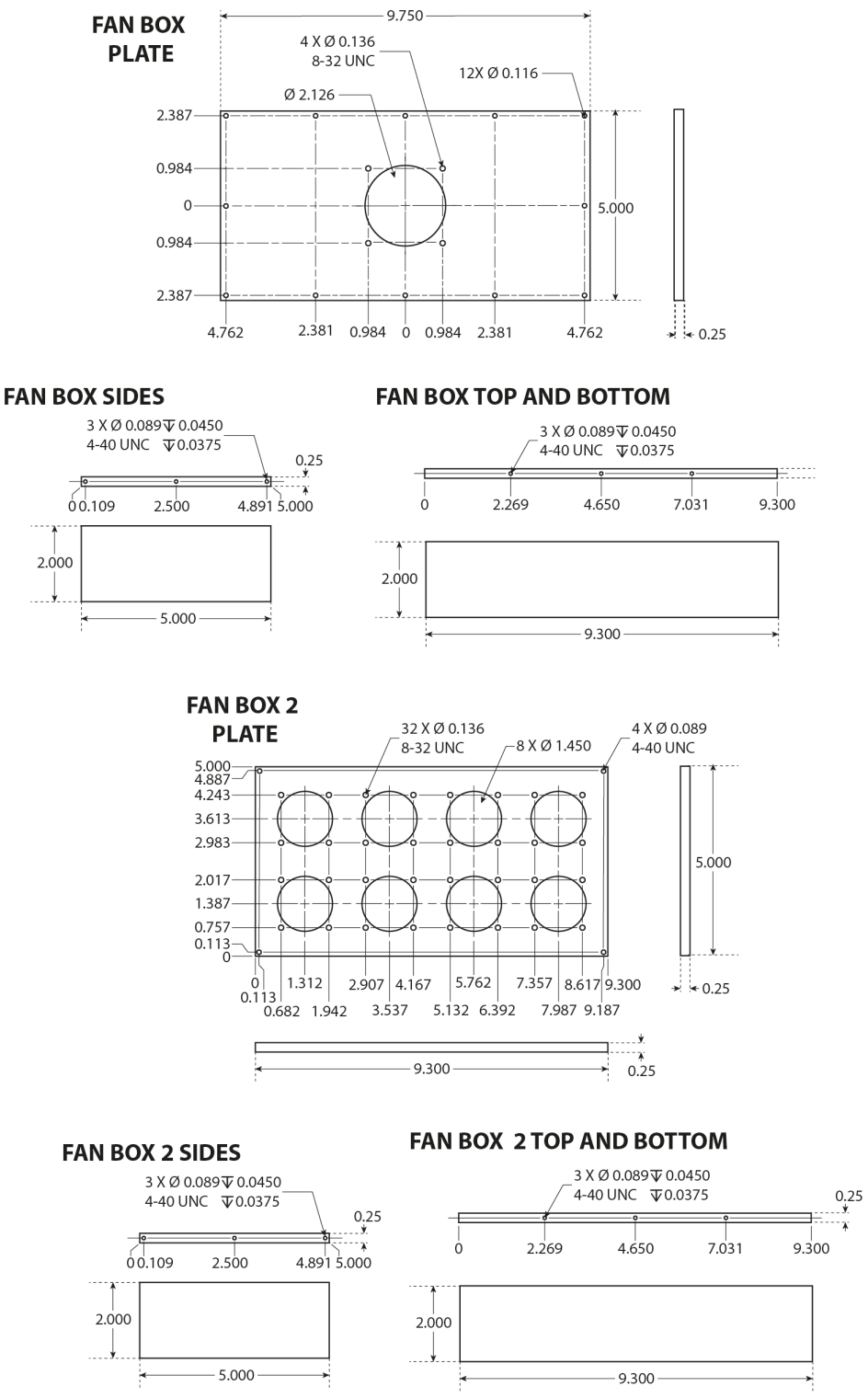

Figure S55. Blueprints of the parts for the fan boxes of the exchanger. All distances are in inches.

Section S5.2. Characterization of the exchanger

- Calculation of the packing porosity of the MOF bed (based on 0.433 kg of sorbent)

Volume of one sorbent bed:

$$V_{bed} = 11.43 \text{ cm} \cdot 11.43 \text{ cm} \cdot 0.3175 \text{ cm} = 41.48 \text{ cm}^3$$

Total volume occupied by the sorbent beds in the exchanger:

$$V_{bed,tot} = 40 \cdot V_{bed} = 40 \cdot 41.48 \text{ cm}^3 = 1659 \text{ cm}^3$$

Total volume occupied by the MOF particles in the exchanger:

$$V_{MOF,p} = \frac{m_{MOF,p}}{\rho_p} = \frac{433 \text{ g}}{0.873 \text{ g cm}^{-3}} = 496 \text{ cm}^3$$

Packing porosity in the exchanger:

$$\phi_{exchanger} = 1 - \frac{V_{MOF,p}}{V_{bed,tot}} = 1 - \frac{496 \text{ cm}^3}{1659 \text{ cm}^3} = 0.701$$

Analogously, the cartridge filled with 433 g Al-fumarate exhibited a packing porosity of 0.693. Thus, the packing porosities used in the device-based experiments are comparable to the packing porosity used during the TGA experiments (Section S4).

- Calculation of the Reynolds numbers associated with the air flow in the exchanger

○ For the desorption phase:

The flow rate was measured using a Model 8346 VelociCalc Air Velocity Meter (TSI Inc.). The apparatus measured the velocity of air (~75 ft min^{-1}) at the exchanger outlet duct (with a cross-sectional area of 0.013 ft^2). Multiplying the velocity by the cross-sectional area afforded a flow rate of ~1 CFM (cubic foot per minute).

$$Q = 1 \text{ CFM} = 0.000472 \text{ m}^3 \text{ s}^{-1}$$

Total cross-sectional area of the six desorption channels:

$$S = 4 \cdot (0.102 \text{ m} \cdot 0.00635 \text{ m}) + 2 \cdot (0.102 \text{ m} \cdot 0.0127 \text{ m}) = 0.00518 \text{ m}^2$$

Air flow velocity in the channels:

$$V = \frac{Q}{S} = \frac{0.000472 \text{ m}^3 \text{ s}^{-1}}{0.00518 \text{ m}^2} = 0.0911 \text{ m s}^{-1}$$

Hydraulic diameter of the channels (slit shape):

$$D_h = 2 \cdot 0.00635 \text{ m} = 0.0127 \text{ m}$$

Kinematic viscosity of air at 100°C:

$$\nu = 2.3 \cdot 10^{-5} \text{ m}^2 \text{ s}^{-1}$$

Reynolds number inside the channel:

$$\mathrm{Re} = \frac{V \cdot D_\mathrm{h}}{\nu} = \frac{0.0911\ \mathrm{m\ s^{-1}} \cdot 0.0127\ \mathrm{m}}{2.3 \cdot 10^{-5}\ \mathrm{m^2\ s^{-1}}} = 50$$

Therefore, the air flow in the exchanger during the desorption phase is laminar, as is the flow used in the TGA experiment (see section S4.2).

- For the adsorption phase:

The flow rate during adsorption could not be directly measured due to the geometry of the adsorption outlet (no exit duct). However, the rating of the desorption fans gives an upper limit to the flow rate (10 CFM). We operate the fan at a voltage slightly above its rating (15 V) for the first few minutes of the adsorption phase, thus, we take a value of 15 CFM as a conservative estimation of the upper limit of the flow rate inside the exchanger (while, realistically, the actual value should be much lower, due to the pressure drop caused by the cartridge):

$$Q_\mathrm{max} = 15\ \mathrm{CFM} = 0.00708\ \mathrm{m^3\ s^{-1}}$$

Total cross-sectional area of the five desorption channels:

$$S = 5 \cdot (0.102\ \mathrm{m} \cdot 0.00635\ \mathrm{m}) = 0.00324\ \mathrm{m^2}$$

Maximal air flow velocity in the channels:

$$V_\mathrm{max} = \frac{Q_\mathrm{max}}{S} = \frac{0.00708\ \mathrm{m^3\ s^{-1}}}{0.00324\ \mathrm{m^2}} = 2.18\ \mathrm{m\ s^{-1}}$$

Hydraulic diameter of the channels (slit shape):

$$D_\mathrm{h} = 2 \cdot 0.00635\ \mathrm{m} = 0.0127\ \mathrm{m}$$

Kinematic viscosity of air at 30°C:

$$\nu = 1.6 \cdot 10^{-5}\ \mathrm{m^2\ s^{-1}}$$

Reynolds number inside the channel:

$$\mathrm{Re_{max}} = \frac{V_\mathrm{max} \cdot D_\mathrm{h}}{\nu} = \frac{2.18\ \mathrm{m\ s^{-1}} \cdot 0.0127\ \mathrm{m}}{1.6 \cdot 10^{-5}\ \mathrm{m^2\ s^{-1}}} = 1700$$

Therefore, we also expect the air flow in the exchanger during the adsorption phase to be always laminar, as is the flow used for the TGA experiment (Section S4.2).

Section S6. Water Harvester

Section S6.1. Preparation and Data Acquisition

The exchanger outlet was connected to a commercial 12 V AC unit acting as a condenser (Model DV1910E-1C 12V Pro from Rigid HVAC Co., LTD) using reinforced plastic tubing with an internal diameter of 1.575 in. The condenser was composed of a mini-compressor (QX1901VDH) cycling a cooling fluid through an insulated cold chamber and a warm radiator. Pictures of the condenser are provided in Figure S56. The water harvester was powered with four 12 V deep-cycle batteries (140 Ah, PHCC Pro Series).

Figure S56. Pictures of the AC unit used as condenser to produce liquid water.

Readings of temperature and RH were collected through a National Instruments data acquisition system (cDAQ – 9174) interfaced with a NI 9205 32-Channel analog input and a NI 9214 16-Channel Isothermal TC Module. The corresponding data was recorded using the software Labview 2016 (National Instruments). Temperature sensors were placed at different locations inside and outside (for ambient condition measurements) of the harvester (Figure S57).

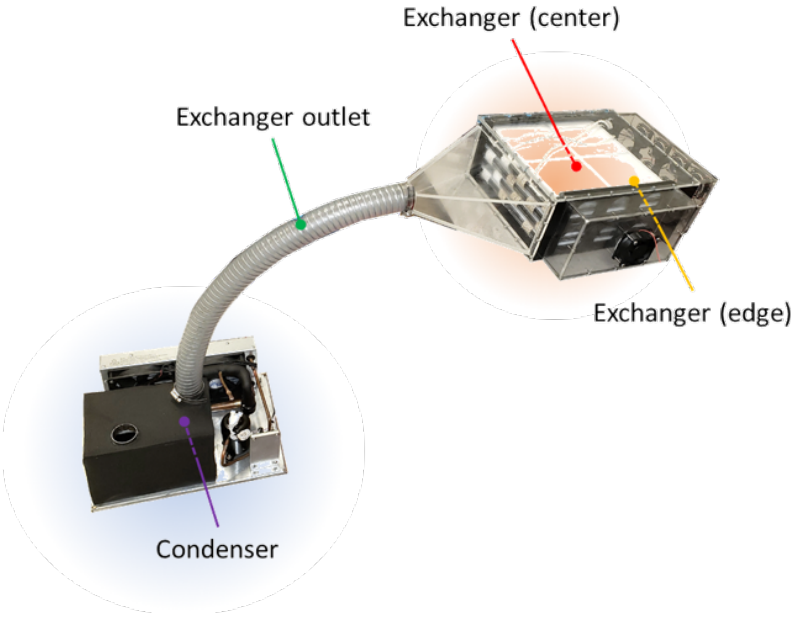

Figure S57. Location of the temperature sensors in the water harvester during operation. A relative humidity sensor is also installed at the exchanger outlet.

The RH was measured using fast-response sensors (Honeywell HIH-4021) containing thermoset capacitive sensing elements. These sensors were calibrated in the 5–90% RH range, at 25 °C and with 5% RH increments, inside a humidity generator (HygroCal100, Michell Inc.). A calibration curve (fitted with a second order polynomial law) was created using the output voltage of the sensors and the RH set by the humidity generator. The temperature was measured using T-type thermocouples (Neoflon PFA, American Wire Gauge 40, OMEGA Engineering). These sensors were calibrated between 15 and 120 °C in increments of 5 °C inside of a dry-well calibrator (Hart Scientific 9103). Around forty data points were collected and averaged at each temperature, with a sampling rate of 5 s, and the calibration data was fitted with a linear function.

Section S6.2. Operation

During the desorption step, the heating strips were powered in parallel with 36 V, and drew 5.8 A of current until the temperature at the center of the exchanger was ~120 °C (although a heat gradient was measured, Figure S58). The heating strips were then switched to a 24 V power supply (now using only two batteries and drawing 3.9 A) to keep the temperature constant inside of the exchanger (Figure 4b). In addition, the eight fans located at the rear of the exchanger were wired in two series-connected groups of four fans, themselves powered in parallel by one 12 V battery (drawing 0.11 A) and switched to 24 V on two batteries as soon as condensation started to appear on the walls of the exchanger (after ~10 minutes, now drawing 0.13 A). The condenser was powered by a different 12 V deep-cycle battery and was drawing about 10 A. The desorption was stopped once the RH in the exchanger outlet reached a constant minimum. The liquid water was collected at the bottom of the condenser through an outlet equipped with a piece of Tygon tubing connected to a glass bottle (Figure 5b-d).

During the adsorption step, only the fan located on the side of the exchanger was powered with a 12 V deep-cycle battery (drawing 0.08 A). The optimal length of the adsorption step was determined using the kinetics measurement reported in Figure 4 and the method presented in Section S7.1.

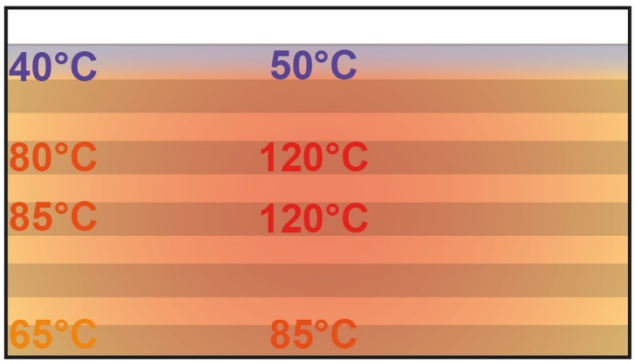

Figure S58. Temperature measured at different points of the central section of the exchanger during desorption. A thermal gradient is observed throughout the cartridge, with a strong decrease in temperature near the top, where the MOF bed is exposed to an empty headspace.

Section S6.3. Power Consumption

The power consumed by each active part of the device can be estimated:

$$P_{\text{heating,initial}} = 36\ \text{V} \cdot 5.8\ \text{A} = 208.8\ \text{W}$$

$$P_{\text{heating,final}} = 24\ \text{V} \cdot 3.9\ \text{A} = 93.6\ \text{W}$$

$$P_{\text{desorption fans,initial}} = 12\ \text{V} \cdot 0.11\ \text{A} = 1.32\ \text{W}$$

$$P_{\text{desorption fans,final}} = 24\ \text{V} \cdot 0.13\ \text{A} = 3.12\ \text{W}$$

$$P_{\text{condenser}} = 12\ \text{V} \cdot 10\ \text{A} = 120\ \text{W}$$

$$P_{\text{adsorption fan}} = 12\ \text{V} \cdot 0.08\ \text{A} = 0.96\ \text{W}$$

The total power consumption for one WHC can be derived from the operating time of each unit.

- For a WHC of 2 hours (one hour of adsorption and one hour of desorption):

$$P_{\text{total,2h-WHC}} = \frac{1}{120\ \text{min}} \cdot [P_{\text{heating,initial}} \cdot 20\ \text{min} + P_{\text{heating,final}} \cdot 40\ \text{min} + P_{\text{desorption fans,initial}} \cdot 10\ \text{min} + P_{\text{desorption fans,final}} \cdot 50\ \text{min} + P_{\text{condenser}} \cdot 60\ \text{min} + P_{\text{adsorption fan}} \cdot 60\ \text{min}] = 128\ \text{W}$$

- For a WHC of 3 hours (two hours of adsorption and one hour of desorption):

$$P_{\text{total,3h-WHC}} = \frac{1}{180\ \text{min}} \cdot [P_{\text{heating,initial}} \cdot 20\ \text{min} + P_{\text{heating,final}} \cdot 40\ \text{min} + P_{\text{desorption fans,initial}} \cdot 10\ \text{min} + P_{\text{desorption fans,final}} \cdot 50\ \text{min} + P_{\text{condenser}} \cdot 60\ \text{min} + P_{\text{adsorption fan}} \cdot 120\ \text{min}] = 86\ \text{W}$$

Based on these two extreme cases, a typical WHC is estimated to consume on average ~100 W. The higher the RH, the faster the adsorption and the higher the consumed power (due to the shorter WHC length used at higher RH), but also the higher the amount of collected water per day.

Section S7. Water Harvesting under Arid Conditions Indoors

Section S7.1. Optimization of the Adsorption Time

An empirical study showed that desorption times typically ranged from 20 min for low loading (this corresponds to the minimum time for water vapor to be released and transferred to the condenser, due to inertia) to 70 min at higher loading (85% of the maximum capacity).
To determine the optimal adsorption time at a given RH, we define the cycle rate as a function of adsorption time t_{ads} and desorption time t_{des}:

$$\text{Cycle rate } (t_{ads}, t_{des}) = \frac{\text{mass of adsorbed water } (t_{ads})}{t_{ads} + t_{des}} \quad \text{(S3)}$$

The mass of adsorbed water as a function of t_{ads} is plotted in Figure 4d. For a given RH, and a given value of t_{ads} the cycle rate depends on t_{des} only, and

$$\text{Cycle rate } (t_{ads}, t_{des} = 20 \text{ min}) \leq \text{Cycle rate } (t_{ads}, t_{des}) \leq \text{Cycle rate } (t_{ads}, t_{des} = 70 \text{ min})$$

This defines a range of cycle rates for each value of t_{ads}, which is illustrated in Figure S59. The optimum adsorption time is then chosen as the time needed to reach the average maximum at each RH (pictured with red crosses on the graph). As a result, the adsorption time is set to 50 minutes for an RH of 40%, to 110 minutes for an RH of 30%, and to 130 minutes for an RH of 20%.

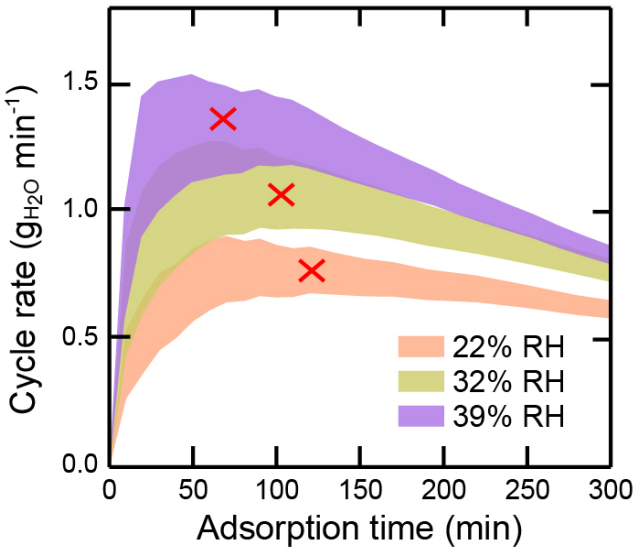

Figure S59. Plot of the range of cycle rates as a function of adsorption time at different relative humidities (RH) and 25 °C. Red crosses represent the average maximum at each RH.

Section S7.2. Water Harvesting Using MOF-303 Indoors under Arid Conditions

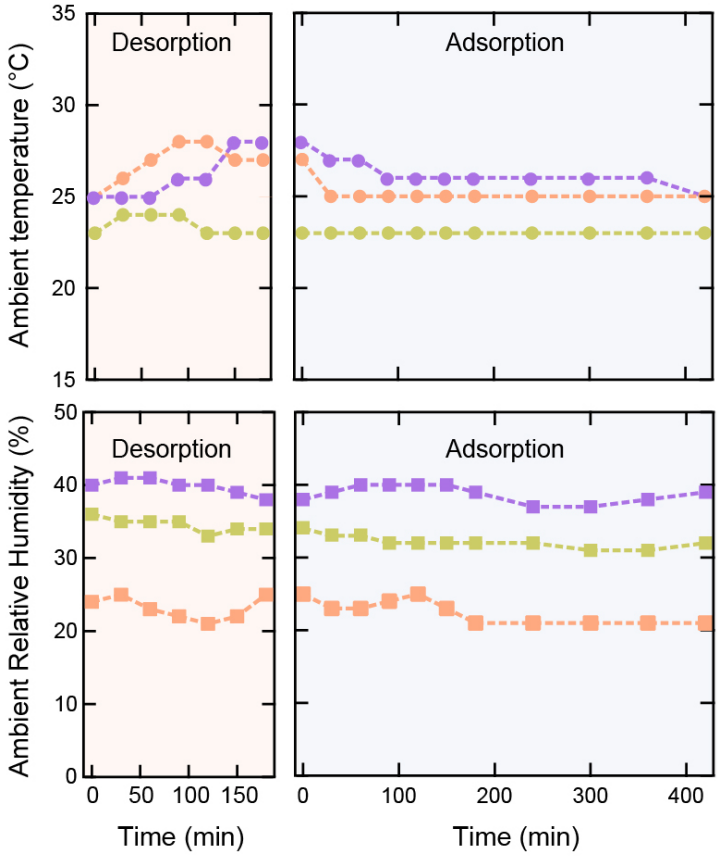

Figure S60. Ambient conditions monitored during the kinetic measurements performed on MOF-303 and presented in Figure 4.

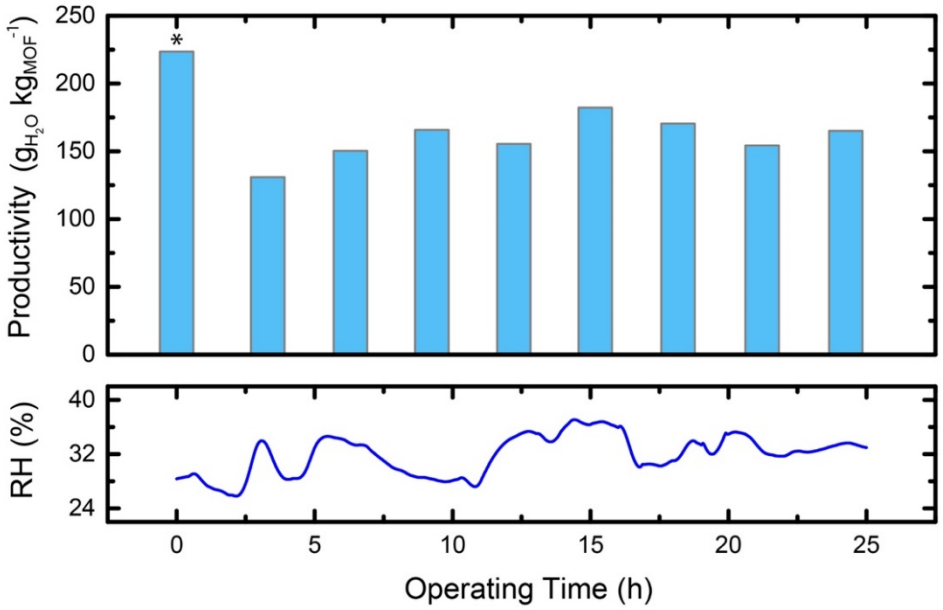

Figure S61. Productivity of the water harvester operated continuously with 433 g of MOF-303 over a period of one day at a temperature of 27 ± 1 °C, displayed alongside the evolution of ambient relative humidity (RH) over the course of the measurement. The productivity of the first WHC (*) is higher because the experiment started with an equilibrated MOF bed.

Section S7.3. Water Harvesting Using Al-Fumarate Indoors under Arid Conditions

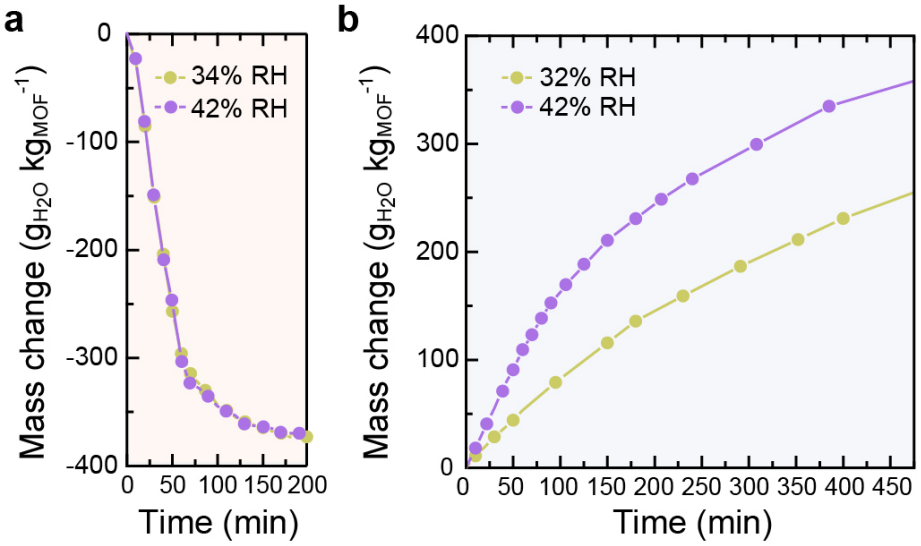

Figure S62. Desorption (a) and adsorption (b) kinetics, in terms of mass of water per mass of MOF against time, measured for Al-fumarate under two different average ambient relative humidities (RH). The evolution of temperature and RH over time are given in Figure S63.

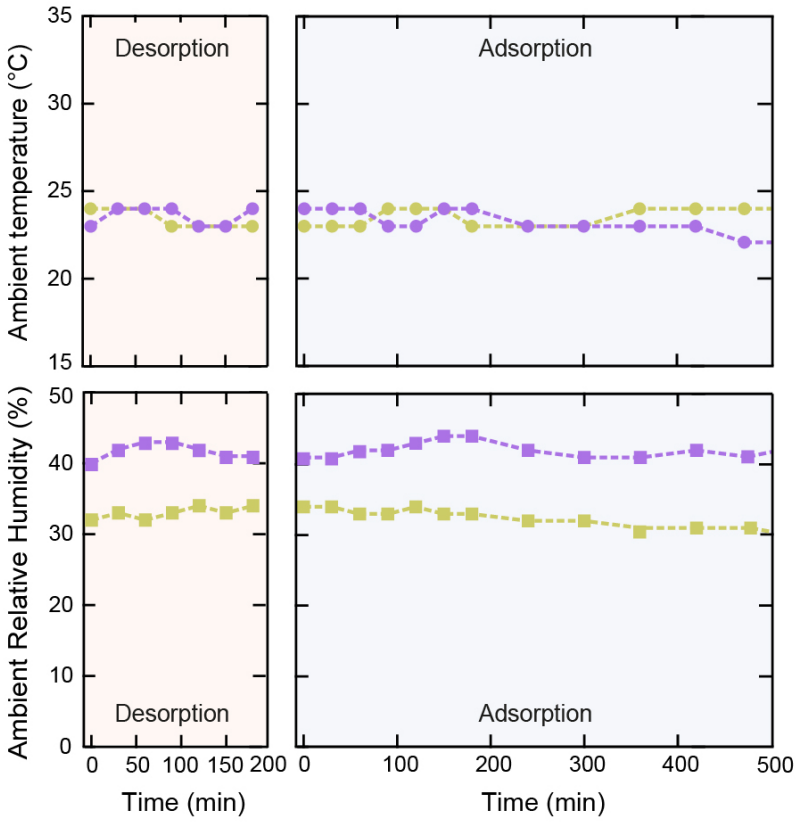

Figure S63. Ambient conditions monitored during the kinetic measurements performed on Al-fumarate and presented in Figure S62.

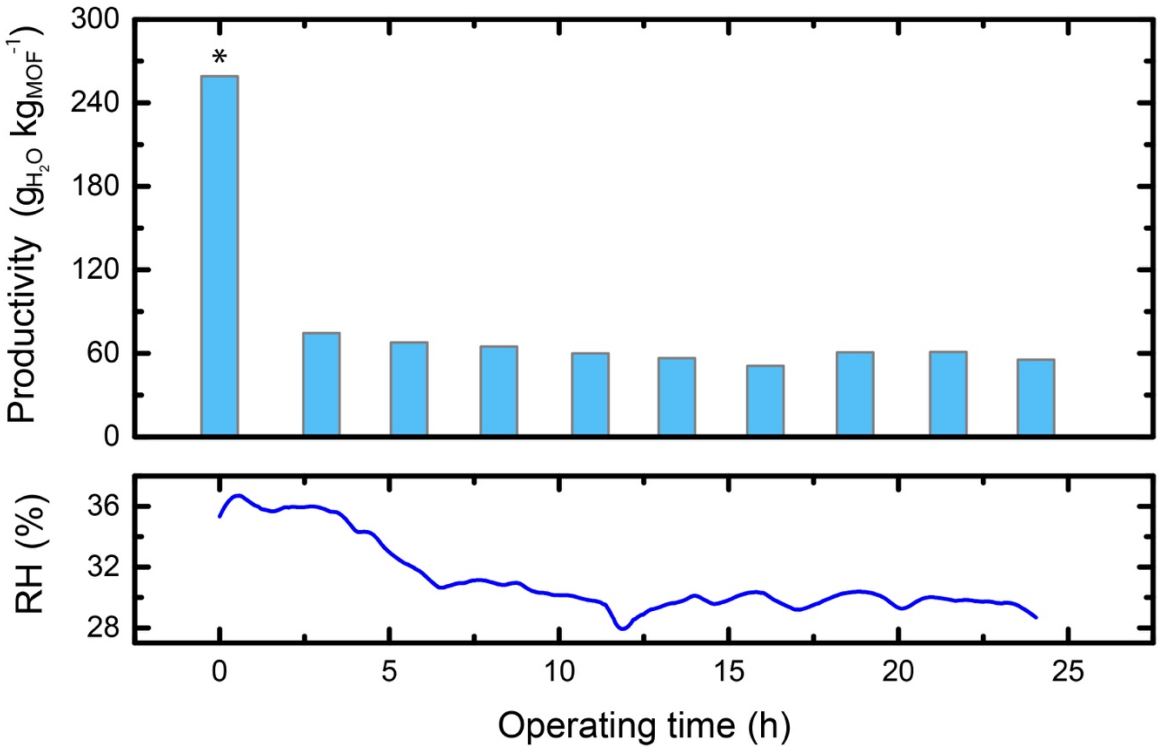

Figure S64. Productivity of the water harvester operated continuously with 433 g of Al-fumarate over a period of one day at a temperature of 23 ± 1 °C, displayed alongside the evolution of ambient relative humidity (RH) over the course of the measurement. The productivity of the first WHC (*) is higher because the experiment started with an equilibrated MOF bed.

Section S8. Water Harvesting in the Mojave Desert

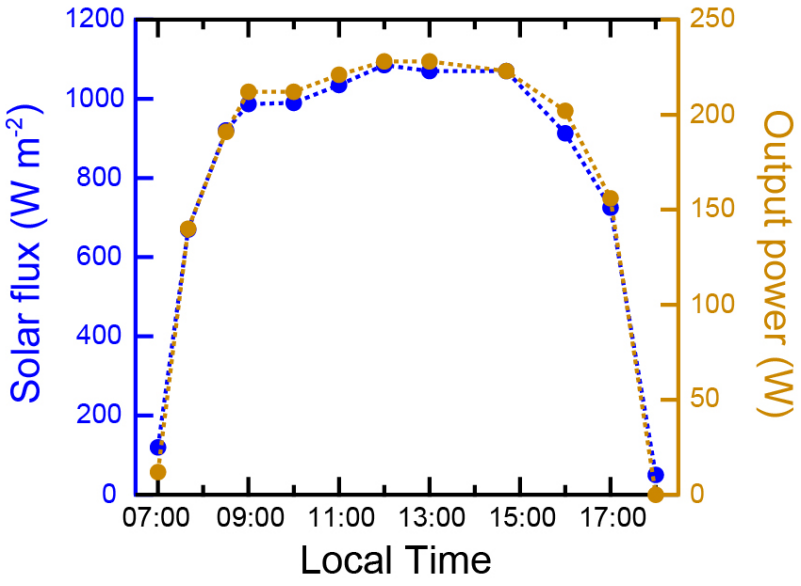

Figure S65. Solar flux and output power measured for the solar module as a function of the time of day at the location of the three-day experiment conducted in the Mojave Desert.

By integration of the data presented in Figure S65, we estimate that each day the solar module delivers:

$$E_{\text{module,1day}} = 2050 \text{ Wh}$$

If we assume the solar module delivers the same amount of energy per day on average, the total energy delivered over the course of the desert experiment was:

$$E_{\text{module,total}} = 6150 \text{ Wh}$$

On the other hand, the average length of a WHC was 2.88 hours (25 cycles over 72 hours). Based on the calculations presented in Section S5.2, we estimate the average power consumption of a WHC to be:

$$P_{\text{WHC,avg}} = 90 \text{ W}$$

And the associated energy consumption to be:

$$E_{\text{WHC,avg}} = 90 \text{ W} \cdot 2.88 \text{ h} = 259 \text{ Wh}$$

The total energy consumed over the course of the experiment was:

$$E_{\text{harvester,total}} = 25 \cdot 259 \text{ Wh} = 6480 \text{ Wh}$$

Therefore, we estimate that the solar module was only able to provide 95% of the total energy consumed over three days. However, the initial charge of the batteries was enough to provide the remaining 5%. A larger module or a more energy-efficient WHC would be necessary for the harvester to operate continuously and off-grid for a more extended time under the same conditions.

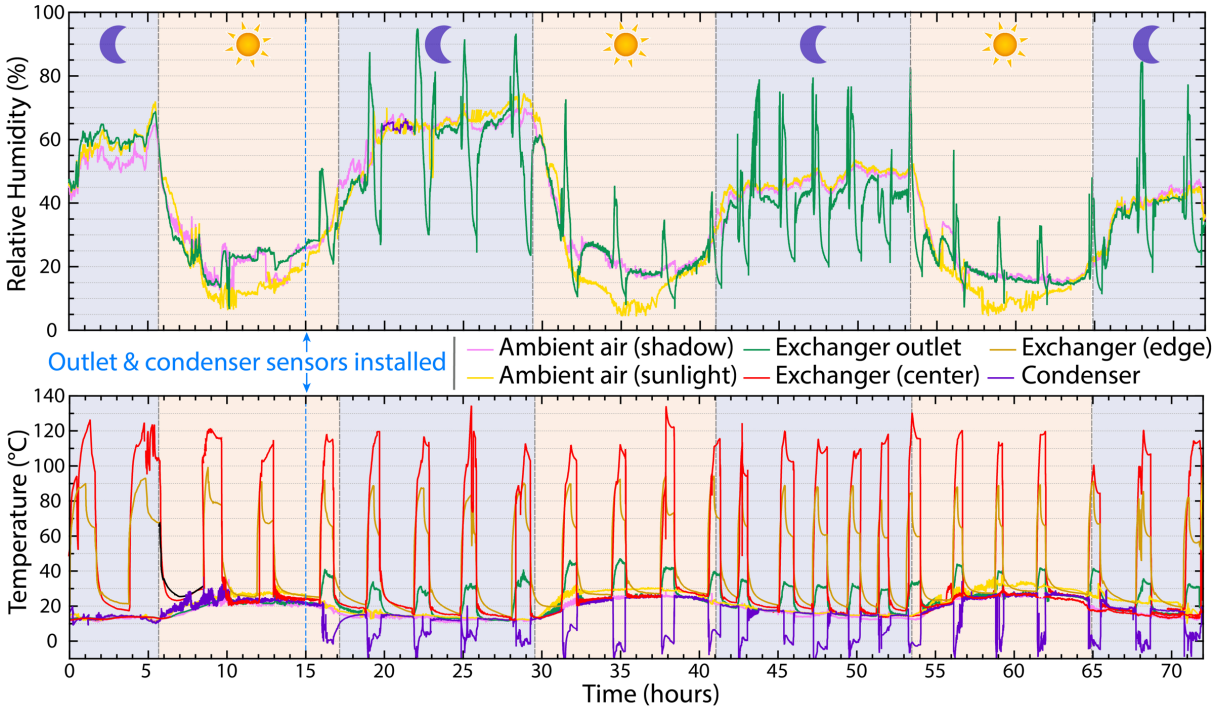

Figure S66. Relative humidity and temperature data collected at different points of the prototype during the three-day experiment conducted in the Mojave Desert. Outlet and condenser sensors were only installed after about 15 hours, as indicated by the blue dashed line.

Section S9. References

(1) Kayal, S.; Chakraborty, A.; Teo, H. W. B. Green Synthesis and Characterization of Aluminium Fumarate Metal-Organic Framework for Heat Transformation Applications. *Mater. Lett.* **2018**, *221*, 165–167.

(2) Kim, H.; Cho, H. J.; Narayanan, S.; Yang, S.; Furukawa, H.; Schiffres, S.; Li, X.; Zhang, Y.-B.; Jiang, J.; Yaghi, O. M.; et al. Characterization of Adsorption Enthalpy of Novel Water-Stable Zeolites and Metal-Organic Frameworks. *Sci. Rep.* **2016**, *6* (1), 19097.

(3) Buck, A. L. New Equations for Computing Vapor Pressure and Enhancement Factor. *J. Appl. Meteorol.* **1981**, *20* (12), 1527–1532.

(4) Gibson, P. W. Effect of Temperature on Water Vapor Transport through Polymer Membrane Laminates. *Polym. Test.* **2000**, *19* (6), 673–691.